Design and construction of an experimental setup for multidimensional spectroscopy in the XUV/ soft-X-ray spectral region

This Master thesis has been carried out by

Marc Anton Alexander Rebholz

at the

Max-Planck Institut für Kernphysik

under the supervision of

Herrn Prof. Dr. Thomas Pfeifer

Design and construction of an experimental setup for multidimensional spectroscopy in the XUV/ soft-X-ray spectral region:

In this work a new transient absorption spectroscopy setup for the extreme ultraviolet (XUV) and soft-X-ray spectral region is introduced. It is based on a four-quadrant split-mirror design which allows to perform four-wave mixing experiments in the mentioned spectral regions. The experimental setup is designed to be operable at high-order harmonic sources as well as free-electron laser (FEL) facilities. The promotion of four-wave mixing spectroscopy to spectral regions with photon energies of several tens of electron volts allows to investigate many new phenomena. Two key examples are the charge-migration dynamics in molecules and the coupling between inner-shell excitations of different types. In this work, first experiments were conducted that serve as a proof of concept for the new experimental design.

Design und Konstruktion eines Experiments zur multidimensionalen Spektroskopie im XUV/ weichen Röntgenbereich:

In dieser Arbeit wird ein neuartiger experimenteller Aufbau vorgestellt, welcher für Transiente-Absorptions-Spektroskopie im extrem ultravioletten Spektralbereich und im schwachen Röntgenbereich ausgelegt ist. Der Aufbau basiert auf einem 4-Quadranten Spiegel, der es erlaubt Vier-Wellen-Misch-Experimente in den aufgeführten Spektralbereichen durchzuführen. Der experimentelle Aufbau ist so konstruiert, dass er sowohl mit Hohen-Harmonischen-Quellen, als auch an Freie-Elektronen-Lasern (FEL) verwendet werden kann. Das Vorantreiben von Vier-Wellen-Misch-Spektroskopie in Spektralbereiche mit Photonenenergien im Bereich von mehreren zehn Elektronenvolt erlaubt es, eine Vielzahl an neuen Phänomenen zu untersuchen. Zwei wichtige Beispiele sind die Dynamik von Ladungstransfers und die Kopplung zwischen verschiedenen Inner-Schalen-Anregungen in Molekülen. In dieser Arbeit wurden erste Experimente durchgeführt, welche als Machbarkeitsstudie für den neuartigen Aufbau dienen.

Contents

1 Introduction

Ever since Eadward Muybridge made a time-resolved measurement of a horse's motion by several triggered cameras [1] scientists tried to record dynamic processes. Since Muybridge's approach using flash photography, there have been made huge progresses in this field. Especially the development of mode-locked lasers that deliver ultrashort pulses with durations down to several femtoseconds ($1\,\mathrm{fs} = 10^{-15}\,\mathrm{s}$) has driven this kind of time-resolved studies to new extremes [2].

Today it is possible to investigate the bound-state dynamics of valence electrons in atoms and molecules. The natural time scale of these processes is on the order of only a few femtoseconds or even in the attosecond regime ($1\,\mathrm{as} = 10^{-18}\,\mathrm{s}$). To probe these dynamics, light pulses with attosecond durations are required. There are two light sources which deliver attosecond radiation with the required intensity and coherence. On the one hand ultra-intense free-electron lasers (FELs) [3], [4] and on the other hand high-order harmonic sources which deliver highly coherent attosecond pulses [5], [6], [7], [8].

Advances in ultrashort pulse generation [9] provided laser pulses with peak intensities in the $10^{14}\,\mathrm{W\,cm^{-2}}$ regime. This made it possible to operate high-order harmonic sources in standard laboratories which promoted the time-resolved investigation of inner-shell electron dynamics [10], [11] as well as the examination and control of correlated electron dynamics [12].

Multidimensional spectroscopy techniques have had a large impact on science and society in the last decades. In the infrared (IR) spectral region multidimensional spectroscopy is applied to measure bond-lengths in molecules, their time-dependent vibrations and even couplings between different bond sites. In the visible (VIS) and ultraviolet (UV) it is used to investigate transitions between different valence electron energy levels in a time-resolved way [13].

The scope of this work was to design and build an experimental setup which promotes multidimensional four-wave mixing spectroscopy to the extreme ultraviolet (XUV) and soft-X-ray spectral region. The high photon energies of these spectral regions allow to

probe time-resolved processes of core-electron transitions. As soon as FELs deliver the sufficient photon energies it is desired to perform four-wave mixing spectroscopy in the XUV/ soft-X-ray spectral region to investigate the coupling of core-electron transitions near specific atomic sites (addressed by their characteristic chemical shifts) in molecules [14]. Additionally it is intended to observe charge-migration dynamics in molecules.

For this purpose a new experimental setup based on a 4-quadrant split-mirror design is presented in this work. With this setup it is possible to split an incident light beam into four identical copies to perform four-wave mixing experiments in the XUV and soft-X-ray spectral regions. Furthermore, first proof of principle experiments are demonstrated.

2 Theoretical background

The process of absorption occurs when electromagnetic radiation, e.g. light, travels through matter. It is one of the most basic processes happening in nature. Therefore it plays a key role in an enormous number of experiments. By investigating the absorption behavior of matter, one can disentangle many aspects of its structure. The scheme of transient-absorption spectroscopy is also used in this work.

The theory of linear absorption can be understood very easily. Assuming the most fundamental microscopic system, a two-level atom, one can explain the key features of absorption. A two-level atom only consists of a ground state $|g\rangle$ and an excited state $|e\rangle$, both of which are eigenstates of the system. If the photon energy is resonant to the transition frequency $\omega_e - \omega_g$, it can be absorbed, leaving the atom in a coherent superposition of the excited state and the ground state. Both states possess a different phase evolution due to their differing energy eigenvalues. This leads to an oscillating dipole moment μ, with a beating frequency equal to the transition frequency. As both states are eigenstates of the system, this dipole oscillation should live forever. However, due to the coupling of the electromagnetic field to vacuum fluctuations, one observes an exponentially decaying dipole oscillation with a characteristic lifetime τ. Fourier-transform connects this exponential decay to the natural absorption line shape, a symmetric Lorentzian profile (see also Figure 2.1). Macroscopically one can observe the attenuation of the light's intensity after passing a certain distance z in the medium. As the absorption of a photon by a single atom occurs several times, the number of photons iteratively decreases while passing the atomic cloud. The intensity of a transmitted light field is directly connected to the number of photons by

$$I = j_{ph} \cdot \hbar\omega, \tag{2.1}$$

with the photon flux density j_{ph}. This leads to the observation of exponential attenuation of the light's intensity while traveling through matter, known as Beer-

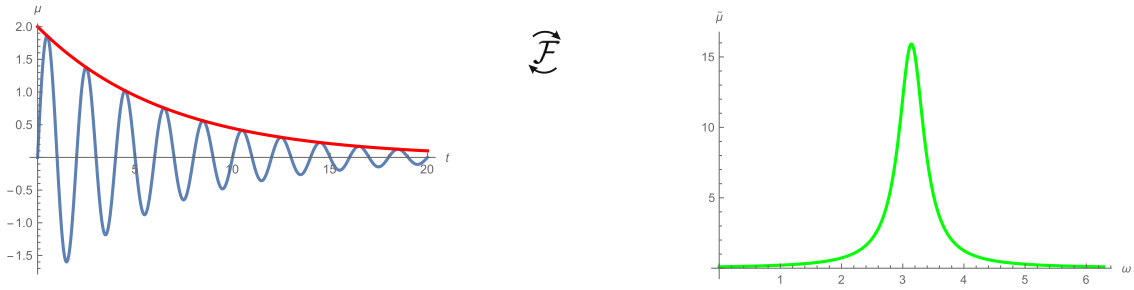

Figure 2.1: Time and frequency representation of the dipole moment of a two-level system excited by a delta-function-like excitation pulse. The Fourier transform connects the temporal decay with lifetime τ with its natural Lorentzian line shape.

Lambert's law

$$\frac{\mathrm{d}I}{\mathrm{d}z} = -\alpha z. \tag{2.2}$$

The absorption coefficient α is in general dependent on the light frequency ω. For a more detailed description see also chapter 2.1.

2.1 Linear Absorption

The classical interaction of an isolated atom with a light field can be described by the displacement $\mathbf{r}$ of the electric charge of the electron e from the nucleus

$$\boldsymbol{\mu} = e\mathbf{r}. \tag{2.3}$$

The hereby induced macroscopic polarization $\mathbf{P}$ of an atomic cloud with number density $\rho_N = \frac{N}{V}$ is

$$\mathbf{P} = \langle \boldsymbol{\mu} \rangle \cdot \rho_N. \tag{2.4}$$

This polarization is induced by the electric field $\mathbf{E}(\omega)$ of the light and is in general frequency dependent

$$\mathbf{P}(\omega) = \epsilon_0 \chi(\omega) \cdot \mathbf{E}(\omega), \tag{2.5}$$

with the dielectric permeability of vacuum ϵ_0 and the dielectric susceptibility $\chi(\omega)$ of the medium. In general $\chi(\omega)$ is a tensor, so that the induced polarization in the medium is not necessarily parallel to the applied electric field. However, only gaseous media are treated in this work. Therefore $\chi(\omega)$ can be considered as a scalar quantity without loosing generality.

Polarization $\mathbf{P}(\omega)$ and electric field $\mathbf{E}(\omega)$ are real quantities, which can in principle

be measured directly. For reasons of mathematical convenience they are treated as complex quantities in the following. As the microscopic dipoles need some time to align in the rapidly oscillating electric field, there is a lag in the dipole response of the medium. This manifests in a phase shift, as is the case for a driven harmonic oscillator. Therefore $\chi(\omega)$ is a complex quantity

$$\chi(\omega) = \chi'(\omega) + i\chi''(\omega). \tag{2.6}$$

It is connected to the refractive index via

$$n^2 = \epsilon_r = 1 + \chi. \tag{2.7}$$

The real part of equation (2.6) accounts for dispersion, whereas the imaginary part relates to absorption. This can be expressed via the absorption coefficient

$$\alpha(\omega) = \frac{\omega}{c} \cdot \chi''(\omega). \tag{2.8}$$

The absorption of light after passing a distance z in a medium then follows Beer-Lambert's law

$$I(\omega, z) = I_0(\omega) \cdot \mathrm{e}^{-\alpha(\omega)z}. \tag{2.9}$$

The macroscopic absorption coefficient $\alpha(\omega)$ connects to the microscopic atomic cross section $\sigma(\omega)$ via

$$\alpha(\omega) = \rho_N \cdot \sigma(\omega). \tag{2.10}$$

With equations (2.4) and (2.5) the atomic cross section can be reformulated as

$$\sigma(\omega) = \frac{1}{\rho_N} \frac{\omega}{c} \cdot \mathrm{Im}\left(\frac{\langle \mu(\omega) \rangle}{E(\omega)}\right). \tag{2.11}$$

In a typical absorption experiment, the intensities $I(\omega, z)$ and I_0 in equation (2.9) are the measured quantities. To evaluate the recorded spectra, one defines the optical density (OD) as

$$\mathrm{OD}(\omega) = \log_{10}\left(\frac{I_0(\omega)}{I(\omega)}\right) = \frac{\sigma(\omega)}{\ln 10} \cdot \rho_N l \tag{2.12}$$

with the sample thickness l.

2.2 Introduction to Fano's original theory

In nature, not only symmetric Lorentzian absorption profiles can be observed. Hans Beutler [15] first observed asymmetric non-Lorentzian absorption profiles in noble gases in 1935. A theoretical description of these profiles was developed by Ugo Fano in 1961 [16]. It relies on the interference between two possible quantum pathways and is not only applicable to absorption, but to several kinds of phenomena.

In the independent-particle approximation (IPA) the wave functions of multi-electron atoms are built up by one-electron wave functions. However there are terms of the Hamiltonian that cannot be accounted for by this approximation. The Coulomb-interaction between different electrons is one of these terms. The total wave function can no longer be written as a product of the one-electron wave functions. As these states of different electronic configurations are entangled, the term configuration interaction (CI) was coined by Ugo Fano.

Above the first ionization threshold one can always find a discrete state $|\varphi\rangle$ which is embedded in a set of continuum states $|\chi_{E'}\rangle$. The energy of the discrete state E_ϕ is degenerate to the continuum energy band E_χ. The Hamiltonian of such a system can be written as

$$\hat{\mathbf{H}} = \begin{pmatrix} \langle\varphi|\hat{\mathbf{H}}|\varphi\rangle & \langle\chi_{E'}|\hat{\mathbf{H}}|\varphi\rangle \\ \langle\varphi|\hat{\mathbf{H}}|\chi_{E'}\rangle & \langle\chi_{E''}|\hat{\mathbf{H}}|\chi_{E'}\rangle \end{pmatrix} = \begin{pmatrix} E_\varphi & V_{E'} \\ V^*_{E'} & E'\delta(E''-E') \end{pmatrix}. \tag{2.13}$$

The off-diagonal element $V_{E'}$ describes the configuration interaction between the discrete state at energy E_φ and a continuum of states with energies E'. Neither the discrete state $|\varphi\rangle$ nor the continuum states $|\chi_{E'}\rangle$ are eigenstates of the system. A new complete basis set of the diagonalized system can be found via

$$|\Psi_E\rangle = a_E\,|\varphi\rangle + \int \mathrm{d}E' b_{EE'}\,|\chi_{E'}\rangle\,. \tag{2.14}$$

To find these new eigenstates, one has to determine the coefficients a_E and $b_{EE'}$. This can be done by solving the equation

$$\langle\Psi_E|\hat{\mathbf{H}}|\Psi_E\rangle = E \tag{2.15}$$

under the normalization condition

$$\langle\Psi_E|\Psi_{\bar{E}}\rangle = \delta(E-\bar{E}). \tag{2.16}$$

The final result [16] then is

$$a_E = \frac{\sin \Delta_E}{\pi V_E} \tag{2.17}$$

and

$$b_{EE'} = \frac{V_{E'}}{\pi V_E} \frac{\sin \Delta_E}{E - E'} - \delta(E - E') \cos \Delta_E, \tag{2.18}$$

with

$$\Delta_E = \arctan \frac{\pi |V_E|^2}{E - E_\varphi - F(E)} \tag{2.19}$$

and

$$F(E) = \mathcal{P} \int \mathrm{d}E' \frac{|V_{E'}|^2}{E - E'}. \tag{2.20}$$

Equations (2.19) and (2.20) represent a phase and energy shift, due to configuration interaction. $\mathcal{P}$ denotes the principal value of the integral. With this, the new eigenstates can be written as

$$|\Psi_E\rangle = \frac{\sin \Delta_E}{\pi V_E} |\Phi\rangle - \cos \Delta_E |\chi_E\rangle . \tag{2.21}$$

The modified bound state $|\Phi\rangle$ is a mixture of the original bound state with continuum states

$$|\Phi\rangle = |\varphi\rangle + \mathcal{P} \int \mathrm{d}E' \frac{V_{E'}}{E - E'} |\chi_{E'}\rangle . \tag{2.22}$$

To further simplify the above expressions, a reduced energy

$$\epsilon = \frac{E - (E_\varphi + F(E))}{\Gamma/2} = \frac{E - E_\Phi}{\Gamma/2} \tag{2.23}$$

with

$$\Gamma = 2\pi |V_E|^2 \tag{2.24}$$

can be introduced. E_Φ marks the energy of the modified bound state, with Γ being the width of the resonance. The odd and even trigonometric functions in equation (2.21) interfere constructively on one side of the resonance energy E_Φ and destructively on the other side. This gives rise to the asymmetric line shape of the resonance (see Figure 2.2). In Fano's original work, a parametrization of the asymmetry was done by comparing the probability of the transition $\hat{\mathbf{T}}$ from the ground state $|g\rangle$ into $|\Psi_E\rangle$

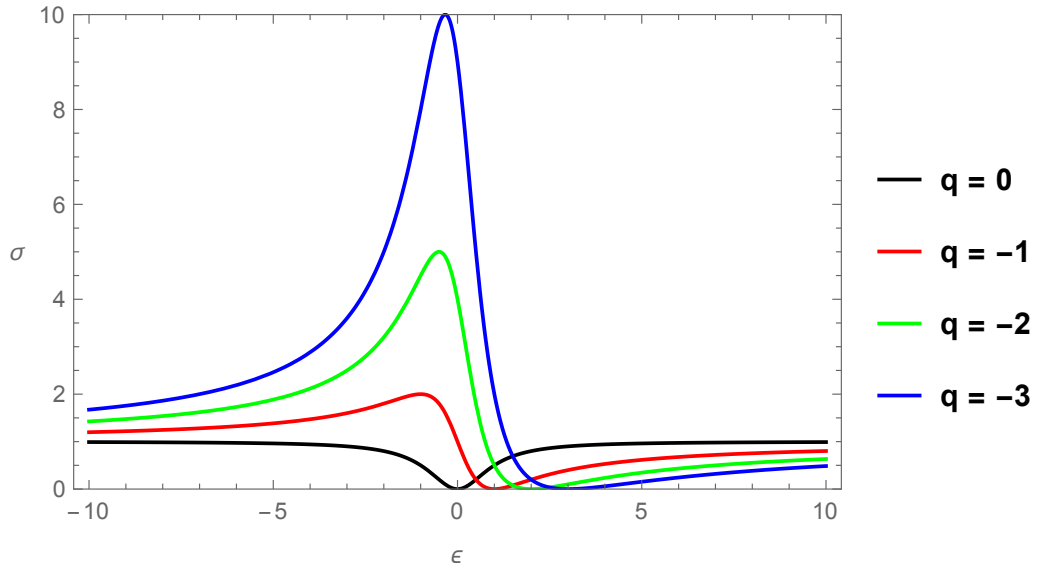

Figure 2.2: Fano absorption profiles for different values of the asymmetry parameter q.

to the probability of the transition into the unperturbed continuum $|\chi_E\rangle$

$$\frac{\left|\langle\Psi_E|\hat{\mathbf{T}}|g\rangle\right|^2}{\left|\langle\chi_E|\hat{\mathbf{T}}|g\rangle\right|^2} = \frac{|q+\epsilon|^2}{1+\epsilon^2}. \tag{2.25}$$

The asymmetry of a line shape is then characterized by the parameter

$$q = \frac{\langle\Phi|\hat{\mathbf{T}}|g\rangle}{\pi V_E^* \langle\chi_E|\hat{\mathbf{T}}|g\rangle}. \tag{2.26}$$

Line shapes for different values of q can be found in Figure 2.2. Experimentally obtained spectra are commonly fitted with

$$\sigma = a \cdot \frac{|q+\epsilon|^2}{1+\epsilon^2} + \sigma_{NR}. \tag{2.27}$$

The parameter a accounts for the relative strength of the resonance compared to an additional non-resonant background σ_{NR}.

2.3 The novel concept of the Fano dipole phase

In his original work Ugo Fano developed a mapping of the asymmetry of a resonance line shape to an asymmetry parameter q. In more recent works [17], [18] a time-

dependent approach was used to investigate and control the asymmetry of atomic resonances. In general a resonance line shape can be characterized in the energy domain by three parameters: position E_Φ, line width Γ and asymmetry q. The linear response of an atomic system to an excitation is described by its dipole response $\tilde{d}(t)$, which is the time-dependent dipole moment of the excited system

$$\tilde{d}(t) \propto c_q \delta(t) + \mathrm{e}^{-\frac{\Gamma}{2}t + i\left[-\frac{E_\Phi}{\hbar}t + \varphi(q)\right]}. \tag{2.28}$$

The time-dependent dipole response does not only consist of the term $c_q\delta(t)$ accounting for the continuum absorption and an exponential decaying term which corresponds to the isolated state absorption, but is phase-shifted by $\varphi(q)$ with respect to the Lorentzian case. A mapping between the asymmetry parameter (2.26) and this phase shift can be found

$$\varphi(q) = 2 \cdot \arg(q - i) \tag{2.29}$$

$$q(\varphi) = -\cot\left(\frac{\varphi}{2}\right). \tag{2.30}$$

An illustrative picture of this $q \leftrightarrow \varphi$ mapping is shown in Figure 2.3. The phase shift with respect to the Lorentzian case can either be introduced by configuration interaction [16], [19] or by inducing an additional phase shift of the excited state. This can be done by dressing the loosely-bound electron in the excited state with an ultrashort laser pulse. This shifts the excited-state energy by the ponderomotive potential

$$U_p = \frac{e^2 E_0^2}{4m\omega^2}. \tag{2.31}$$

It is dependent on the strength of the laser field E_0 and its frequency ω. Classically it is the additional kinetic energy an electron possesses due to the quivering motion it performs in the laser field. The energy shift alters the phase evolution of the excited state through the quantum mechanical connection of phase and energy. A phase shift compared to the undisturbed case is accumulated during the duration T of the laser pulse

$$\Delta\varphi = \int_0^T \frac{U_p}{\hbar}\,\mathrm{d}t. \tag{2.32}$$

The total phase of the excited state then reads

$$\varphi = \frac{E_\Phi}{\hbar} \cdot T + \Delta\varphi. \tag{2.33}$$

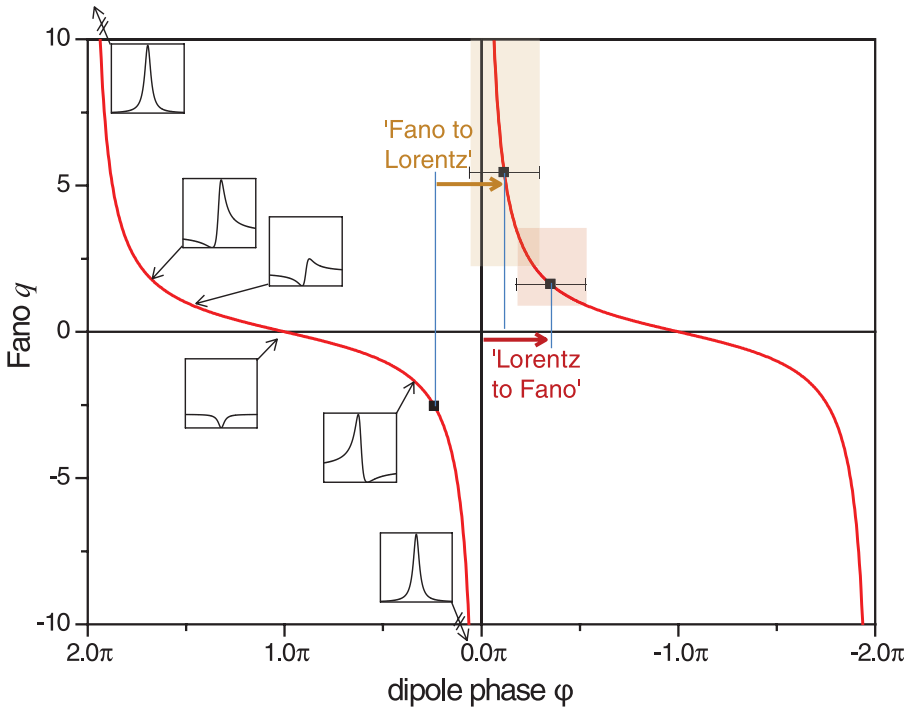

Figure 2.3: Shown is the mapping between Fano's asymmetry parameter q and the dipole phase φ. In the extreme case $q \to \pm\infty$ and $\varphi \to 2n\pi$ the line shape is Lorentzian. For the other extreme $q \to 0$ and $\varphi \to (2n+1)\pi$, window resonances appear. In between the characteristic Fano line shapes can be found. The arrows mark the pioneering experiment [17] where both transitions from Lorentz to Fano as well as from Fano to Lorentz lines were observed. This figure is reprinted from [17].

By controlling either the intensity [17] (Figure 2.4) or the instant of turning on the dressing field [18] one can therefore control the so-called dipole phase of the system.

2.4 Four-wave mixing

In general, the relation between applied electric field and macroscopic polarization of a medium does not have to be linear. The most universal relation is of the form

$$\mathbf{P}(\mathbf{E}, t) = f(\mathbf{E}(t)). \tag{2.34}$$

This can be expanded into a Taylor series with coefficients $\chi^{(i)}$ for a medium that responds instantaneously to applied electric fields, e.g. no resonances of the medium

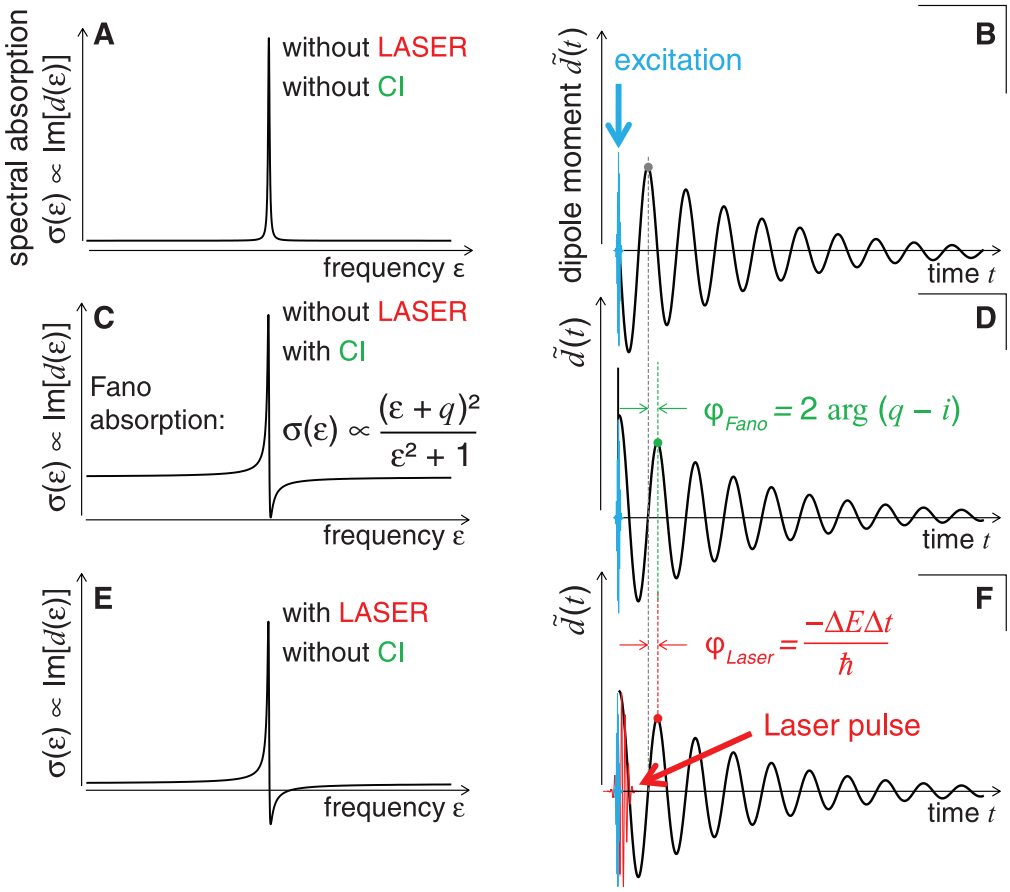

Figure 2.4: The left columns shows different kinds of dipole responses of an atomic system after excitation in the spectral domain. The right column shows the corresponding time-dependent dipole responses. (a,b) show the undisturbed Lorentzian dipole response of an atom after excitation. (c,d) show the dipole response of an atom that arises due to the phase shift from configuration interaction. (e,f) show the dipole response after phase-shifting the dipole response with a strong laser field. This figure is reprinted from [17].

are driven by the external electric field

$$\mathbf{P}(\mathbf{E},t) = \chi^{(1)}\mathbf{E}(t) + \chi^{(2)}\mathbf{E}^2(t) + \chi^{(3)}\mathbf{E}^3(t)\ldots. \tag{2.35}$$

The nonlinear polarization components lead to nonlinear terms in the wave equation

$$\nabla^2\mathbf{E} - \frac{1}{c^2}\frac{\partial^2\mathbf{E}}{\partial t^2} = \frac{1}{\epsilon_0 c^2}\frac{\partial^2\mathbf{P}}{\partial t^2} \tag{2.36}$$

and therefore to the generation of new frequency components in the signal. The second order term leads to three-wave mixing and is the cause of the Pockels effect.

Due to symmetry reasons, it can only be observed in crystals without inversion symmetry. In the gaseous media under investigation in this work, only third- or higher-order nonlinear effects can be observed. As the absolute value of the nonlinear susceptibilities decreases with their order, only third-order nonlinear effects shall be treated here. These are the (self-induced) Kerr-effect which leads to self-phase modulation (SPM) and the process of four-wave mixing (FWM).

When an electric field with three different frequency components ω_i irradiates a sample, one can treat it as a superposition of three waves with different frequencies. The first wave with frequency ω_1 generates a polarization grating in the sample. The second wave ω_2 interferes with this grating which generates components at the sum $\omega_1 + \omega_2$ and difference $\omega_1 - \omega_2$ frequencies. The third wave then interferes with the original frequencies, as well as with their sum and difference frequency which generates the fourth field ω_4. In the most general case the incident fields have different directions $\mathbf{k_i}$ as well as different frequencies ω_i. Furthermore the susceptibility is a tensorial quantity, so that the polarization response of the medium depends on its orientation relative to the direction of the electric field. The third-order polarization response of the medium then reads [20]

$$\begin{aligned} P_i^{(3)}(\omega_4, \mathbf{r}) = \frac{1}{2}\epsilon_0 \chi_{ijkl}^{(3)}(-\omega_4, \omega_1, -\omega_2, \omega_3) E_j(\omega_1) E_k^*(\omega_2) E_l(\omega_3) \\ \cdot \exp[i(\mathbf{k_1} - \mathbf{k_2} + \mathbf{k_3}) \cdot \mathbf{r} - i\omega_4 t] + c.c.. \end{aligned} \tag{2.37}$$

Due to energy and momentum conservation, additionally

$$\omega_4 = \omega_1 - \omega_2 + \omega_3 \quad \text{and} \quad \mathbf{k_4} = \mathbf{k_1} - \mathbf{k_2} + \mathbf{k_3}. \tag{2.38}$$

have to be fulfilled. The generated FWM-signal is emitted into another direction $\mathbf{k_4}$ as the incident waves, which can also be seen in Figure 2.5. This can be used to easily separate the weak signal field from the strong excitation fields. There are further, more sophisticated, ways to ensure momentum conservation or phase-matching. For further information refer to [21] and [22].

2.5 High-order harmonics generation

To excite the inner shell dipole transitions investigated in this work, radiation with photon energies on the order of several electron volts is needed. To probe these

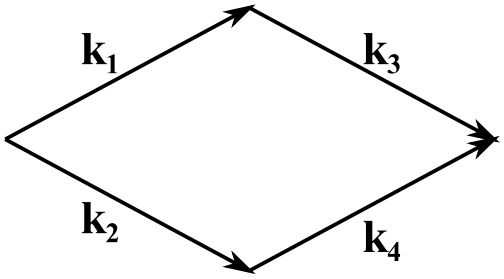

Figure 2.5: Phase-matching condition for non-collinear four-wave mixing.

transitions on their natural time scale, light pulses with durations on the order of attoseconds ($1\,\mathrm{as} = 10^{-18}\,\mathrm{s}$) are required. There are two kind of sources which produce coherent radiation within this energy range with adequate pulse durations and sufficiently high intensities. On the one hand free-electron lasers (FELs) which are large-scale facilities and on the other hand high-harmonic sources that can be operated as table-top systems in a standard laboratory. In the scope of this work, only high-harmonic sources shall be treated, however in principle the conducted experiments are also possible with FEL sources (see also section **??**).

High-order harmonic generation (HHG) is a highly nonlinear process of light–matter interaction. However it can be understood in a classical picture using Newton's equations [8]. The atom can be ionized in three different ways. For relatively weak electric fields the atom can absorb many photons which leads to the ionization of one electron. For stronger electric fields the atomic potential gets skewed so that it forms a tunneling barrier (see also Figure 2.6). Part of the electron wave function can tunnel out. For even stronger fields, the electron can overcome the barrier without tunneling. The parameter which determines the different regimes was introduced by Leonid Keldysh in 1965 [23]. It describes how fast the electron's response is, compared to the oscillation of the laser electric field

$$\gamma = \sqrt{\frac{I_p}{2U_p}}. \tag{2.39}$$

I_p describes the ionization potential of the electron bound by the atomic core. The ponderomotive potential U_p quantifies the strength of the laser electric field. For $\gamma \ll 1$, the electronic response is much faster than the oscillation of the laser field. Therefore, the electron may tunnel through the formed potential barrier. For $\gamma \gg 1$, the laser field oscillates much faster than the electron's response time. In this case,

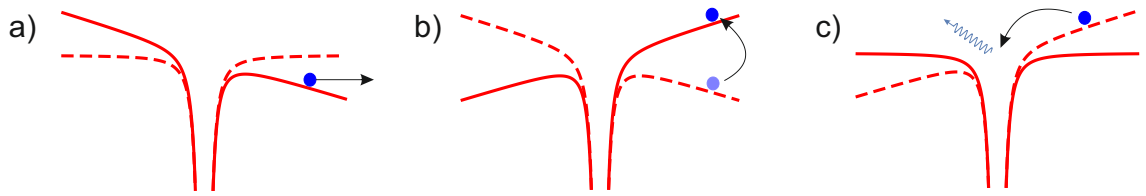

Figure 2.6: a) Step 1: The electron is being ionized under the influence of the strong laser field. b) Step 2: The laser field changes its sign after one half-cycle $T/2$. The electron turns around and may perform a re-colliding trajectory. c) Step 3: Upon recombination the electron releases its additional kinetic energy in form of a high-energetic XUV photon. XUV light bursts are being emitted at each half-cycle of the laser electric field. There is a phase shift of π between each emitted light pulse. This leads to the production of only odd-order harmonics.

multiple photons can be absorbed to ionize the electron.
After the ionization process, the free electron can be treated as a classical charged particle. It is driven away from the parent ion by the laser field. After one half-cycle the laser field changes its sign so that electron is driven back towards the atomic core. There are recombining and non-recombining trajectories. When recombining with its parent ion, the additional kinetic energy of the electron is emitted in form of one high-energetic photon (see also Figure 2.6)

$$\hbar\omega_{HHG} = E_{kin}^{(r)} + I_p. \tag{2.40}$$

Due to the nature of the generating process, the high-harmonic spectra observed in experiments [8] possess a broad plateau of equally intense energies, as well as a sharp cutoff at the highest photon energy. The plateau originates in the similar probabilities of recombination for a range of photon energies. At the point of re-collision, the electron can only acquire kinetic energy up to a certain limit due to the oscillating nature of the laser field. In the classical trajectory approximation, the sharp cutoff of photon energies is therefore related to the ponderomotive potential (2.31)

$$\hbar\omega_{HHG,max} = 3.17U_p + I_p. \tag{2.41}$$

3 Design and construction of the experiment

In this work a novel experimental setup for multidimensional coherent spectroscopy in the extreme ultraviolet (XUV)/ soft X-ray spectral region is being presented. The extension of the widely used multidimensional spectroscopy scheme to this spectral region promises new insights into electronic dynamics like charge migration between different atomic sites in molecules. However, bringing two-dimensional spectroscopy into the XUV and soft X-ray spectral region is challenging due to the lack of standard optical components at these photon energies. To the best of our knowledge, a comparable setup has not yet been realized.

In a precursor transient-absorption spectroscopy setup [24] at the MPIK, Heidelberg, it is possible to generate attosecond extreme ultraviolet (XUV) pulses via high-harmonic generation (HHG) of a sub-10 fs near-infrared (NIR) pulse from a Titanium-doped Sapphire (Ti:Sa) laser. A time delay between the generated XUV pulse and the co-propagating NIR pulse is introduced using a split-mirror setup. Additionally, the intensity of the NIR light is controlled by a motorized aperture. With this setup two-dimensional transient absorption spectroscopy experiments were performed [17], [25] which provide insight into time-dependent electronic processes in atomic and molecular systems. In the previous work, the focus was placed on measuring autoionizing wave packet dynamics in helium [12], the laser-induced control and manipulation of doubly-excited state line-shapes in helium and a new time-domain understanding of Fano's original theory [17]. Also, a two-dimensional spectroscopy representation of coupling dynamics in strong fields has been developed [18]. Analogously to the traditional two-dimensional spectroscopy, this approach spreads the spectral information onto a two-dimensional spectral map.

The presented new beamline features a refined design, based on a 4-quadrant split-mirror setup, allowing to split the used light pulses into 4 identical copies. A time delay between each of these pulses can be introduced. This provides the potential to

perform various new experimental schemes, also including traditional four-wave mixing two-dimensional spectroscopy, but now up to XUV photon energies. To that end the beamline is designed to be operable at both attosecond HHG sources and ultra-intense free-electron laser (FEL) facilities. The corresponding site selectivity achieved by using XUV light will enable the observation of charge migration, even on attosecond time scales as soon as FELs deliver short enough pulses, or high-harmonic sources deliver the required intensities for attosecond-pump–attosecond probe schemes.

A complete design view of the experimental setup can be found in Figure 3.1. Its individual components will be presented in the following.

3.1 The femtosecond laser system

The basic working principle of a LASER (**L**ight **A**mplification by **S**timulated **E**mission of **R**adiation) relies on the principle of stimulated emission. To drive a laser, a gain medium which is pumped to achieve population inversion by means of electrically, optically or even chemically driving transitions in the gain medium. Furthermore some kind of feedback that allows for efficient amplification is needed. This is realized by an optical resonator. The most successful laser type in recent years was the titanium-doped sapphire laser (Ti:Al_2O_3 or Ti:Sa) which is also used in this work. For more detailed information on this and other types of lasers refer to textbooks like [22] or [26]. The reason for its success is its broad, nearly octave-spanning gain profile which is centered around 800 nm. As the duration of a laser pulse and its spectrum are directly connected by Fourier-transformation this leads to very short laser pulses on the order of ten femtoseconds ($1\,\mathrm{fs} = 10^{-15}\,\mathrm{s}$). Ultrashort laser pulses like these are needed for the experiments performed in this work due to their high intensities in the order of $10^{14}\,\mathrm{W\,cm^{-2}}$ when focused down to typical spot sizes of 50 µm. This allows to efficiently drive the nonlinear processes investigated in this work.

The commercial laser system *Femtopower compact Pro CEP* from *Femtolasers* was employed in this work. It consists of the laser oscillator *Rainbow* which delivers sub-10 fs pulses at a repetition rate of 80 MHz with pulse energies in the nanojoule ($1\,\mathrm{nJ} = 10^{-9}\,\mathrm{J}$) regime. Since pulse energies in the millijoule ($1\,\mathrm{mJ} = 10^{-3}\,\mathrm{J}$) regime are required to drive the highly-nonlinear processes used in this work, a chirped-pulse amplifier (CPA) is used to amplify the pulses to a pulse energy of roughly 0.7 mJ. The amplifier uses a multi-pass configuration to amplify the laser pulses. To prevent the damage of optical elements inside the amplifier or the Ti:Sa crystal itself, the

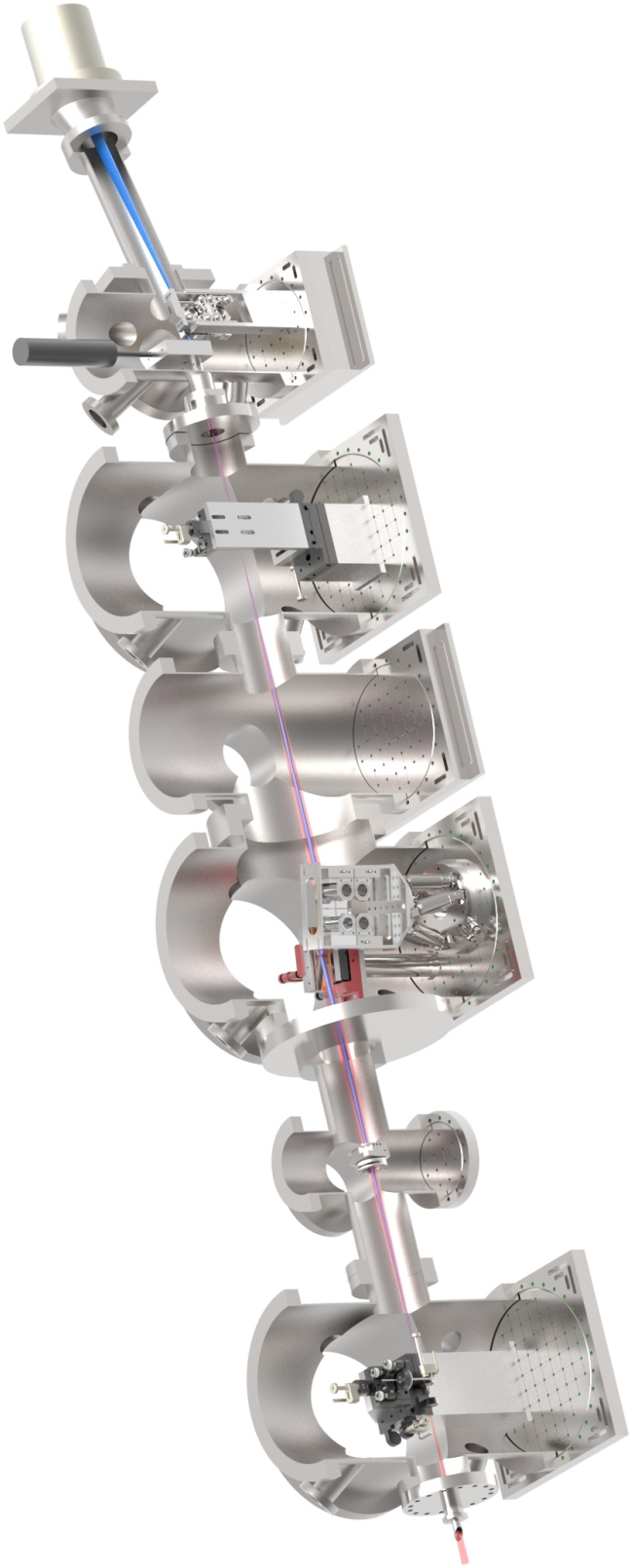

Figure 3.1: A complete representation of the experimental setup. Its individual components will be presented in the following.

femtosecond oscillator pulses are stretched to several picoseconds ($1\,\mathrm{ps} = 10^{-12}\,\mathrm{s}$) by letting them propagate through a slab of fused-silica glass. A Pockels cell (see also section 2.4) after the fourth pass through the amplifier crystal is used to select only every 20000th oscillator pulse to prevent the system from thermal damage. This reduces the repetition rate of the system from 80 MHz down to 4 kHz. Essentially the high repetition rate is traded for higher pulse energies. The centermost parts of the spectrum are amplified most efficiently leading to gain-narrowing inside of the amplifying medium. This results in a decrease in the bandwidth of the amplified pulses. The pulses finally are recompressed to their new bandwidth limit of sub-30 fs in a prism compressor. To get even shorter pulses their spectrum has to be broadened, again. Therefore they are focused into a hollow-core fiber with a core diameter of 100 µm which is filled with roughly 2.5 bar of Neon. Due to the high intensities at this low spot size several nonlinear processes occur inside the fiber, with self-phase modulation (SPM) being the most important one (see section 2.4). After passing the fiber the pulses pass through a chirped-mirror (CM) compressor, consisting of 8 chirped mirrors. These mirrors add negative group delay dispersion (GDD) to the pulses to compensate for the positive GDD introduced by propagation through air and other optical components. The chirped mirrors are additionally designed to compensate for the higher-order dispersion terms. This allows to compress the pulses close to their bandwidth limit. After the chirped-mirror compressor two fused-silica glass wedges are set up in the beam path to variably add positive dispersion to the pulses, in case too much negative dispersion was introduced by the chirped mirrors. Optimizing the dispersion, pulses with a duration of sub-7 fs and a pulse energy of approximately 0.3 mJ can be achieved this way. These pulses are then available to drive high-order harmonic generation and to conduct the desired experiments.

3.2 High-order harmonics generation cell

To carry out the experiments on inner-shell excitations of atoms performed in this work, electromagnetic radiation with photon energies of several tens of electron volts is needed to resonantly drive these transitions. Furthermore, a high spectral bandwidth is crucial to coherently excite a complete Rydberg series of states in order to investigate the dynamics of the induced wave packet. The pulse duration has to be short compared to the lifetime of the states which is on the order of femtoseconds. Since no laser systems are available which deliver these photon energies in combination

with attosecond pulse durations, high-order harmonic generation (see section 2.5) is used to get the required photon energies. To realize this, the high-intense ultrashort laser pulses are focused into the high-order harmonics generation cell (see Figure 3.2). The actual generation cell is a stainless-steel tube with 100 µm-holes drilled in the front and back face. The laser beam is focused into these holes. The steel tube is filled with noble gases with backing pressures of tens of millibars in which the process of high-order harmonics generation takes place (see section 2.5). Three translation stages which are equipped with picomotor actuators [27] are used to remotely move the cell along all three axes. In the direction of the beam a translation of 5 cm is possible to ensure proper phase matching. Perpendicular to the beam axis a translation of 2.5 cm is possible which is sufficient to move the cell into the beam path or to move it completely out of the beam path if necessary. A rotation mount allows for fine adjustment of the rotation and the tilt of the steel tube.

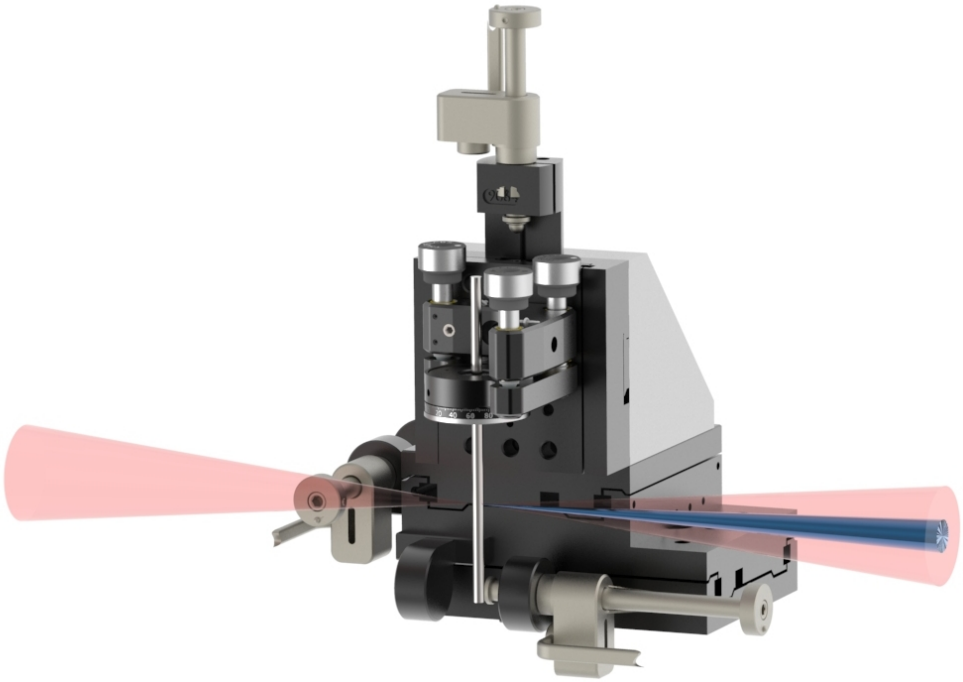

Figure 3.2: The home-built high-order harmonics generation cell. It consits of the actual steel cell mounted in the rotation mount and three translation stages with picomotor actuators. Also shown is the NIR laser beam which is focused into the cell and the outgoing NIR and XUV beams.

The experimental cell in which the actual experiments are conducted is built in a similar way. Small differences in geometry had to be made for lack of space inside of the vacuum housing (see also Figure 3.1).

3.3 Intensity control

To adjust the intensity of the NIR beam one can exploit the difference in the divergence of the NIR ($\sim 15\,\mathrm{mrad}$) and the XUV beam ($\sim 1\,\mathrm{mrad}$). As its wavelength is much longer for a similar source size, the NIR beam also possesses a much larger divergence angle. The outer part of the NIR beam can be cut out by an aperture without influencing the XUV beam, thereby continuously tuning its intensity (see Figure 3.3). This allows using the NIR intensity as a dynamical control parameter in the experiment. One key experiment is the laser control of absorption line shapes in Helium [17].

The setup used for this purpose is a home built motorized iris aperture. It consists of a closed-loop rotation stage and a zero-aperture iris attached to the inner, rotating, part of the closed-loop stage using a home-built adapter. To translate the ultra-precise positioning of the closed-loop rotation stage onto the iris diaphragm, the iris lever is fixed inside the vacuum chamber. Hysteresis effects originating from the zero-aperture iris diaphragm have to be considered by driving the apparatus unidirectionally. Intensity scans should therefore always be performed from fully open to closed or the other way round. Openings from fully closed to a diameter of 2.5 cm can be reached with this setup, allowing for full control of the NIR intensity. A position of 0° of the rotation stage corresponds to a completely open iris aperture and a position of 90° corresponds to a fully closed iris aperture.

3.4 Toroidal mirror

To refocus the XUV and NIR beams for experiments at high intensity, the solution is to image the high-order harmonics generation cell into the experimental cell. To achieve a high throughput for the XUV light for a broad band of energies, grazing incidence reflection off a metal surface is favored. In order to fulfill these prerequisites, a gold-coated toroidal mirror with a focal length of $f = 350\,\mathrm{mm}$ is used under 15° grazing incidence. An imaging ratio of 1:1 was chosen as it minimizes aberrations. This can be reached using a $2f$–$2f$ imaging geometry. The selected angle of incidence ensures a reasonably high reflectivity for the XUV radiation and at the same time

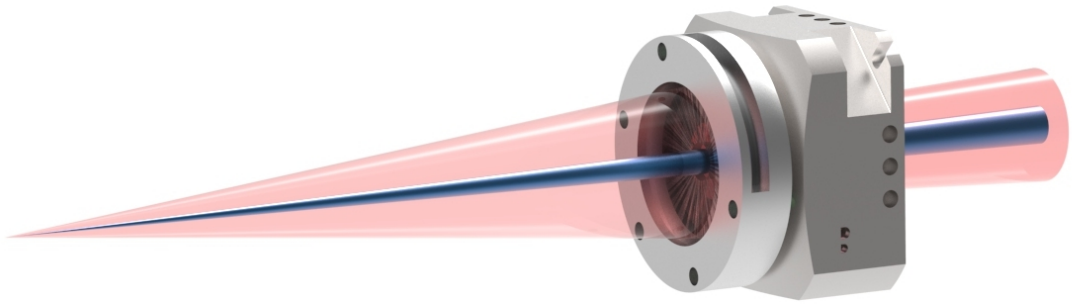

Figure 3.3: Home-built motorized iris aperture. It consists of a closed-loop rotation stage and a zero-aperture iris.

allows for precise alignment of the toroidal mirror to reduce aberrations as much as possible.

To align the toroidal mirror at its final position inside the vacuum chambers, a motorized five-axis aligner was used in combination with a motorized mirror mount (see Figure 3.4, Figure 3.5).

In the following the steps to align the toroidal mirror correctly and thereby reduce aberrations are described. The initial alignment of the mirror is best made outside of the vacuum chambers to have easy access to the mirror and to guarantee for the incident beam to be perfectly parallel to the optical table. Also, a laser with good beam profile, e.g. a HeNe laser, should be used to be able to evaluate the minimal astigmatism. The mode of the Ti:Sa after the hollow-core fiber can be very different from an ideal Gaussian mode which makes it hard to appraise a perfect image of the beam spot. A sketch of the adjustment screws of the toroidal mirror and their effect can be found in Figure 3.5.

As a first step the alignment beam should be aligned parallel to the optical table as in every proper alignment procedure. The toroidal mirror is to be mounted in a way that it is hit in the center by the alignment beam. The mirror should then be illuminated in the center. With the set screw D it has to be tilted so that the reflected beam is again parallel to the optical table. Subsequently the mirror has to be illuminated only in a small spot on one end. With the set screws A'/B' its height on that side should be adjusted so that the reflected beam is of the same height as the incident beam. The same should be done with the other end of the mirror.

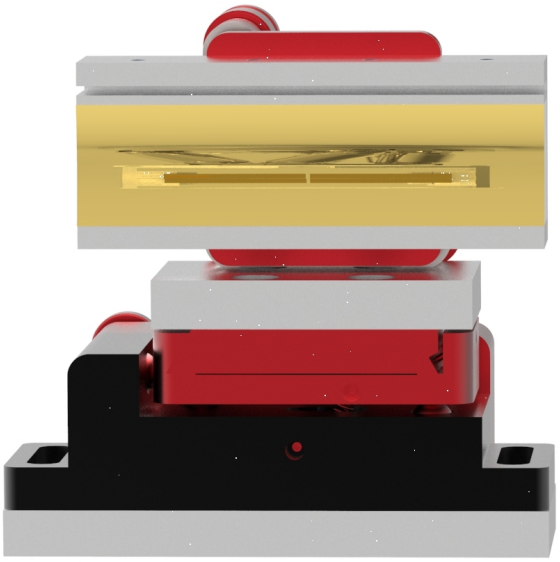

Figure 3.4: Toroidal mirror with motorized mount. As a reflection in the mirror, the 4-quadrant split-mirror setup (see section 3.5) can be seen.

This ensures a rough alignment of the mirror parallel to the optical table. The fine alignment is done iteratively by minimizing the astigmatism as is described in the following. At this point, the mirror has to be placed at its final position in the vacuum chamber because the following steps would have to be repeated when moving the mirror. It is crucial to have a proper beam path prior to the toroidal mirror since only for this beam path a perfect image can be reached in the future. The toroidal mirror should be placed in the beam path and its image has to be monitored in the far field. The mirror is to be moved by hand so that the image is symmetrical, there is no clipping but at the same time the mirror is illuminated completely. The following steps then have to be performed iteratively until the astigmatism is minimized.

1. Place camera (beam profiler preferred) near the focus of the toroidal mirror, in the middle between sagittal and tangential focus.

2. Tilt the mirror with set screw C until the intensity in the focus is maximized. This guarantees that the mirror is hit under an angle which is very similar to the desired 15° which it was designed for.

3. Move the camera from sagittal to tangential focus. If the ellipses are not perfectly horizontal and vertical but tilted, the mirror is not entirely parallel to the optical

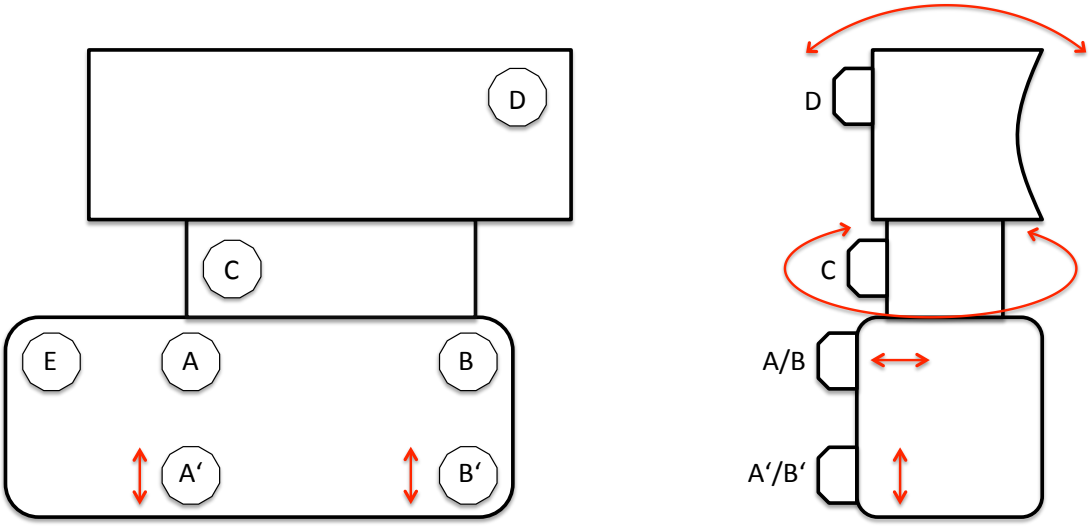

Figure 3.5: Shown is a sketch of the motorized mount of the toroidal mirror. It consists of a picomotor 5-axes aligner and mirror mount (see also Figure 3.4). The set screws A, A', B, B' and E belong to the 5-axes aligner, the set screws C and D belong to the mirror mount. The set screws A' and B' allow for individual height adjustment of each end of the mirror and are used to align it parallel to the optical table. The set screws A and B enable to move the mirror orthogonal to its surface when operated simultaneously or to rotate the mirror when operated individually. To decouple these two movements, the set screw C of the mirror mount is used to rotate the mirror. The set screw D of the mirror mount allows to tilt the mirror. The set screw E enables the translation of the mirror parallel to its surface.

table. Adjust this with the set screws A'/B' until the ellipses are perfectly horizontal and vertical.

4. In case the vertical beam path was altered by the previous step, readjust it with set screw D.

For other imaging geometries than 1:1 additional coma will occur. This complicates the proper judgment of the astigmatism. Therefore the correct placement of the toroidal mirror alongside the beam path has to be ensured.

3.5 The 4-quadrant split-mirror

The presented 4-quadrant split-mirror is the essential component of the new beamline design. It provides the ability to split the incident beam into four time delayed but otherwise identical copies. This is achieved by a setup consisting of 4 rectangular gold-coated mirrors (see Figure 3.6). The system is designed for the operation in

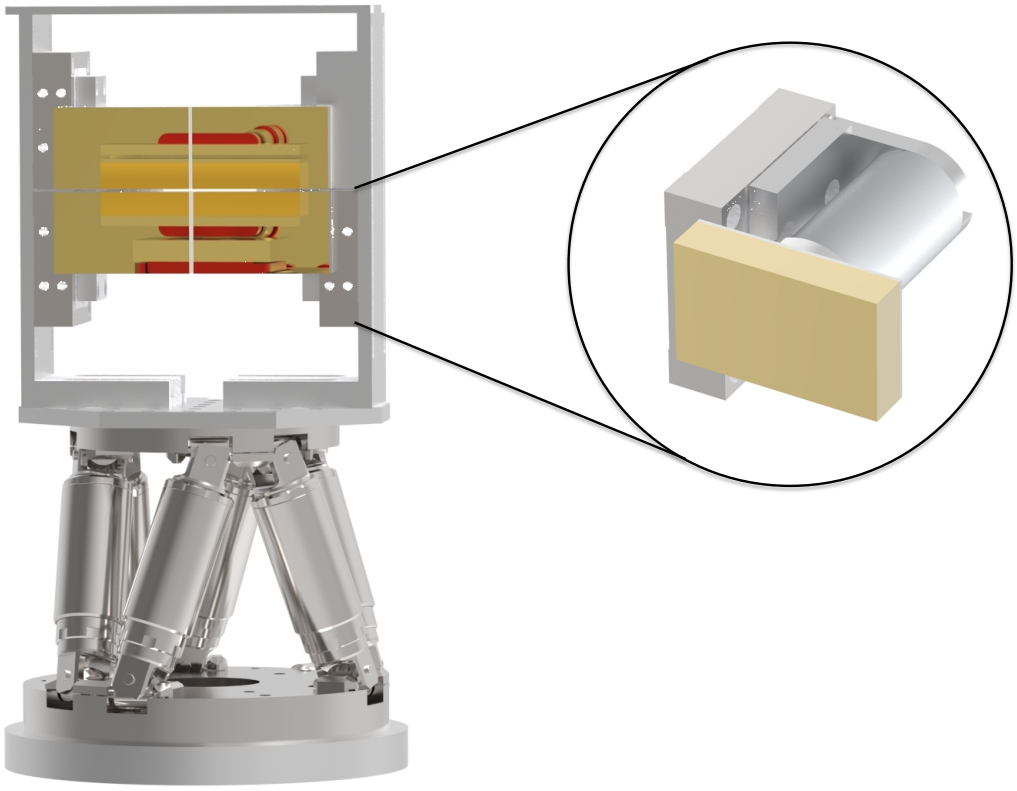

Figure 3.6: 4-split mirror system consisting of one fixed mirror and 3 dynamic mirrors. In the reflection, the toroidal mirror that sits opposite to the 4-split mirror can be seen. The detail shows one segment of the split-mirror. It is built of a linear translation stage, a tip/tilt stage (cylindrical) which is used to compensate for the offset in the interaction region and the gold mirror itself.

two different experimental modes: (i), attosecond transient absorption spectroscopy (ATAS) with several temporally independent XUV pulses obtained via HHG in combination with several few-cycle NIR pulses. And (ii), ultra-intense FEL-based XUV pulses for (conventional) two-dimensional spectroscopy experiments. Three of the mirror segments are mounted on piezo-driven linear stages to introduce a time delay between the four pulses. The stages offer a maximal translation of 250 µm which translates into a maximal time delay of 431 fs under 15° grazing incidence. The step size of the stages is specified as 1 nm which would translate into a resolution of ≈ 2 as. Vibrations of the turbo molecular pumps and other flaws in the stability of the experiment (e.g. unstable beam pointing) are expected to decrease this resolution. Nevertheless a very high time resolution can be reached with these delay stages. Under gracing incidence a small displacement of the mirror segments will lead to a parallel

offset of the beams in the interaction region. To compensate for this, the dynamic mirrors are additionally mounted on tip/ tilt stages (see detail in Figure 3.6). These provide a total tilt of 4 µrad in both axes with a step size of 0.05 µrad.

At free-electron laser facilities it is important to be able to accommodate to varying FEL beam conditions. In case the beam pointing of the FEL beam changes, it is important to have the possibility to realign the split-mirror system as a whole. To ensure that the beam path after the split-mirror system isn't altered in this case, the whole system is mounted onto a hexapod positioning system. This allows to align the beam in a way that it follows the same path every time. A hexapod system was chosen for this purpose as it guarantees high precision as well as long-term stability which is crucial for the planned experiments.

Attosecond transient absorption spectroscopy with three temporally independent pulses

The experiments that preceded this work made use of an broadband XUV pulse that creates a coherent superposition of several atomic states (a wave packet), followed by an NIR pulse that disturbs that time-dependent excited system. The most straightforward excitation sequence for first experiments with the new setup consequently consists of a single XUV pulse followed by two NIR pulses (see Figure 3.7). By now varying

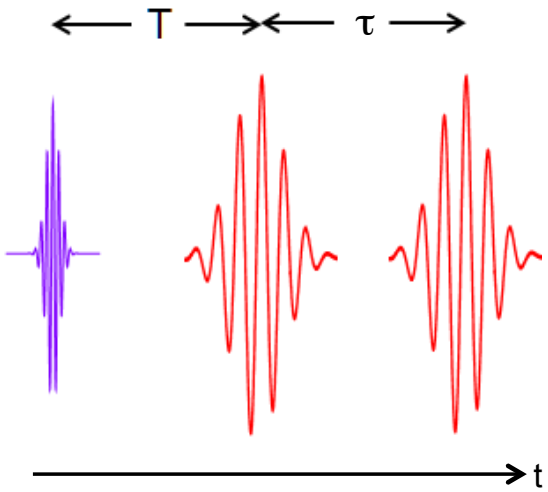

Figure 3.7: One possible excitation sequence feasible with the new mirror system. One XUV pulse is followed by two NIR pulses. This scheme generates a FWM signal in the target, which can be brought to interference with the second copy of the XUV pulse for heterodyne detection.

the time delay τ between the two NIR pulses, the spectrum which disturbs the wave packet can be shaped in a desired way. Figure 3.8 shows the spectrum of three different configurations of NIR pulses. The topmost row shows the spectrum of a single NIR excitation pulse, whereas the lower two rows show the excitation spectra for a two-pulse configuration with different time delays. The strong dependence of the excitation spectrum by this pulse delay can be seen. This way it is for instance

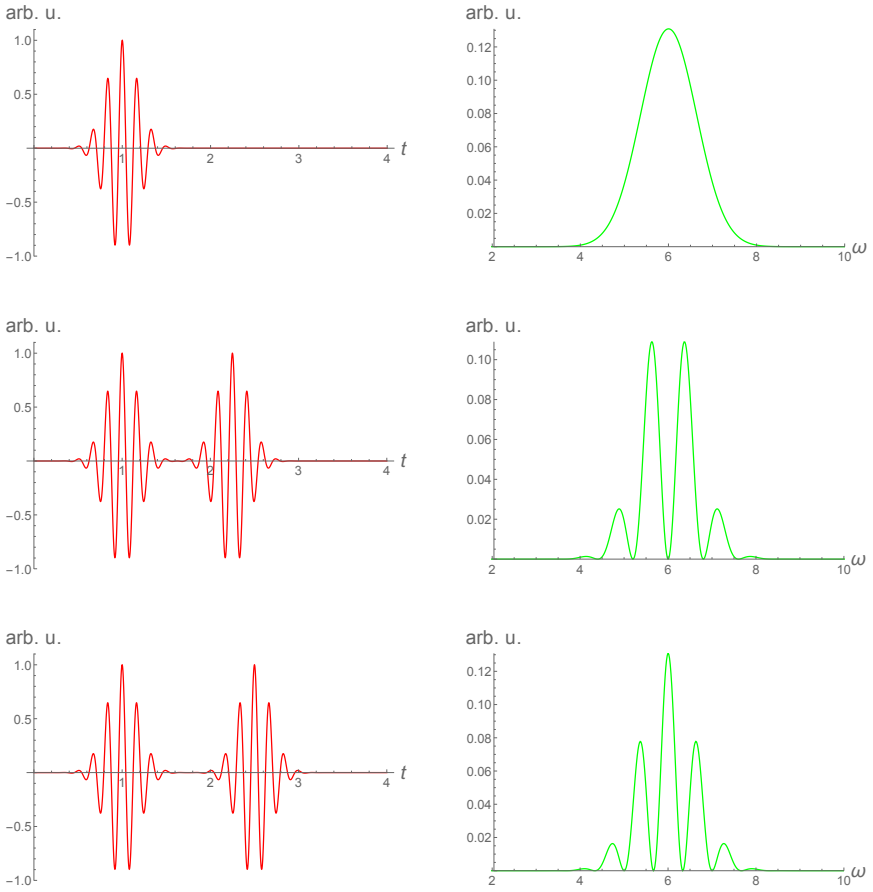

Figure 3.8: The different NIR excitation sequences and their associated spectra. The first row shows a single-pulse excitation with its continuous spectrum. The second row shows a two-pulse excitation sequence with a time delay that leads to several spectral peaks with a central dip. Another time delay in the third row also leads to several spectral peaks but with a central maximum. This way two excited states with an energetic difference equal to the central energy in the spectrum could be coupled or decoupled by shaping the excitation spectrum.

possible to actively turn the coupling between two excited states which is induced by the NIR pulses [28] on or off.

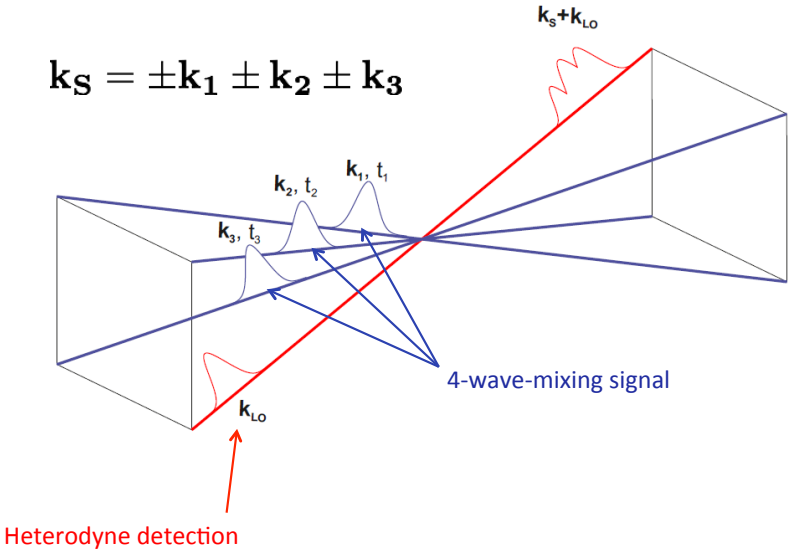

Figure 3.9: Sketch of the non-collinear FWM scheme. The first three pulses $\mathbf{k}_1$, $\mathbf{k}_2$, $\mathbf{k}_3$ generate the FWM signal $\mathbf{k}_S$ which is emitted into the direction that is given by the phase-matching condition $\mathbf{k}_s = \pm\mathbf{k}_1 \pm \mathbf{k}_2 \pm \mathbf{k}_3$. The fourth pulse $\mathbf{k}_{LO}$ is called the local oscillator. It is used to phase-sensitively detect the FWM signal.

Four-wave mixing and two-dimensional absorption spectroscopy

In the infrared spectral region two-dimensional absorption spectroscopy (2-DAS) is widely used for structural analysis of large molecular compounds. It is very similar to the magnetic-resonance imaging (MRI) technique which operates at radio frequencies. The transfer of this technique to photon energies in the XUV spectral regions promises to give information about the time-resolved electronic dynamics, specific to certain elements near their core-absorption edges, of atoms and molecules. This information could lead to advances in atomic physics and physical chemistry beyond imagination, as electronic excitations could eventually be tracked with attosecond resolution as they spread and relocalize throughout molecules. It is therefore highly desired to promote this transfer to XUV photon energies. The scope of this work was to design and build an experimental setup which allows for this kind of experiments.

Figure 3.9 shows the excitation scheme of non-collinear four-wave mixing (FWM). The first three excitation pulses generate the FWM signal in the sample (equation (2.37)) and the fourth pulse is used as a so-called local oscillator which allows for phase-sensitive heterodyne detection of the signal. The time delay between two (or

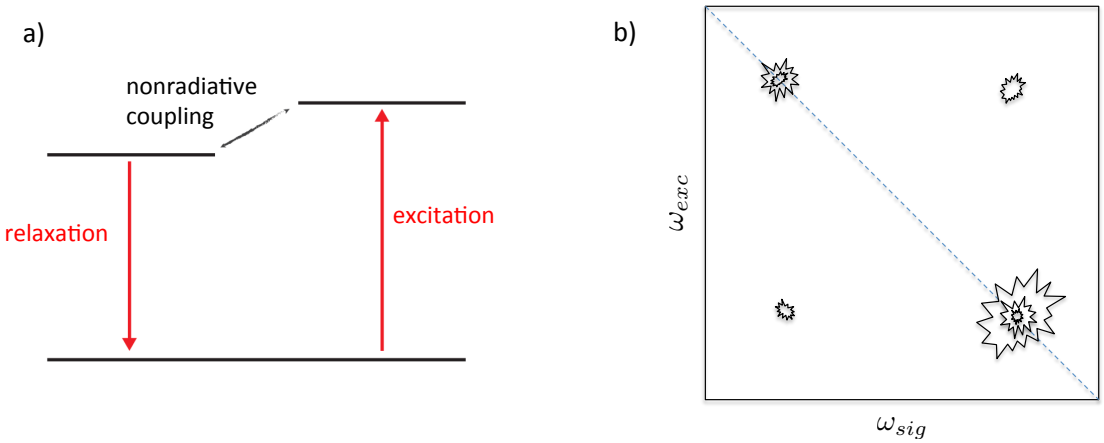

Figure 3.10: a) shows a sketch of a three-level scheme that experiences non-radiative coupling between the two excited states. b) shows a typical two-dimensional absorption spectrum that is generated by a level scheme like that.

more) of the exciting pulses is then varied to shape the excitation spectrum and the emitted signal is recorded for different time delays τ. Fourier transformation over the time-delay axis leads to a second energy axis that is called Fourier-energy axis. A two-dimensional representation of the signal with two energy axes is then possible with one axis being the Fourier-energy ω_{exc} and the other the photon energy spectrum directly measured with the detector ω_{sig} (see Figure 3.10 b)). The signal components on the diagonal (blue dashed line) are the same components that can also be found in linear absorption spectroscopy. Off-diagonal components indicate coupling between different states which, for instance, share the same ground or excited state. An example is shown in Figure 3.10 a). It consists of two excited states that experience non-radiative coupling and share the same ground state. If now one of the states is excited with a resonant photon (ω_{exc}) the population can be transfered to the other upper state level by the non-radiative coupling. When the system then relaxes to its ground state again, a photon with another energy ω_{rel} is being emitted. This leads to the appearance of a cross peak. There doesn't necessarily have to be a physical coupling between the excited states. Excited state absorption (absorption of an additional photon which raises an electron to a higher lying state) and ground state depletion (if there is no more electron in the ground state, absorption cannot happen) also lead to the emergence of cross peaks.

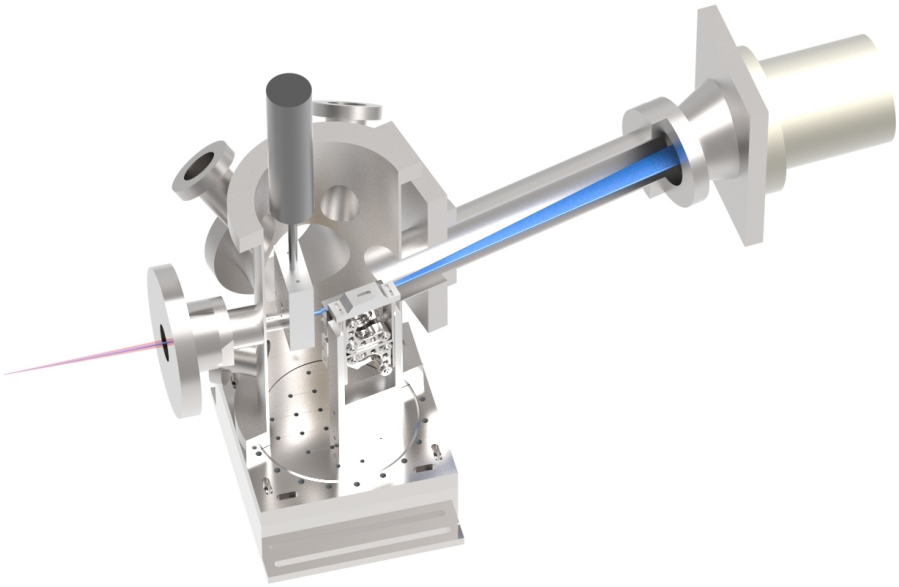

Figure 3.11: Image of the high-resolution flat-field XUV spectrometer. A filter construction allows to effectively filter out the NIR radiation which would otherwise damage the camera using a thin-foil metal filter. The XUV radiation is then dispersed and imaged onto a flat-field image plane of 110 mm width by a concave VLS grating. The XUV spectrum is then being detected by a thermo-electrically cooled back-illuminated CCD camera. The camera chip covers 26.8 mm of the total flat-field image. To detect the whole spectral region of interest, the camera is mounted in a mechanical bearing (not shown) that allows to move the camera parallel to the image plane.

3.6 High-resolution flat-field XUV spectrometer

In this section the high-resolution flat-field XUV spectrometer used in this work is introduced. The design of this spectrometer is adopted from the design in [24] as it has proven to be an ideal setup for the conducted experiments. An image of the spectrometer design can be found in Figure 3.11. The home-built spectrometer consists of a concave variable line spacing (VLS) grating with an average groove density of 1200 mm^{-1}. This grating is designed to disperse a wavelength range from 11 nm to 62 nm (corresponding to a photon energy of 20 eV to 120 eV) onto a flat image plane of 110 mm length. This image is then detected with a back-illuminated CCD camera that is sensitive to the photon energies of interest. The noise level of the camera can be reduced by cooling its sensor thermo-electrically. The CCD chip of the camera consists of 1340 × 400 pixels of 20 × 20 µm size. The camera chip can therefore cover 26.8 mm of the total image plane of 110 mm length. To detect the

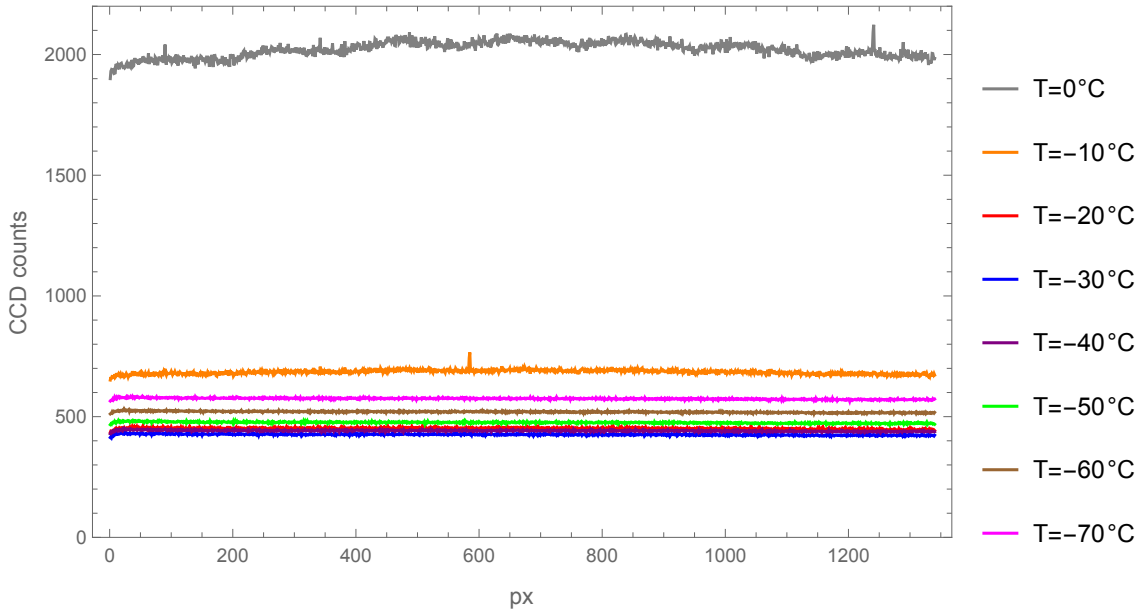

Figure 3.12: Temperature dependence of the noise level of the XUV camera. The noise level reaches its minimum at −30 °C.

total spectral range, the XUV camera is mounted on a mechanical bearing which allows to move the camera alongside the grating's flat field. This allows to position the camera with high precision to detect every spectral region of interest with high resolution. An estimation yielded a theoretical spectral resolution of 27 meV (s.d.) for an XUV photon energy of 60 eV [24].

In Figure 3.12 the temperature dependence of the noise level of the XUV camera is being presented. A clear drop of the noise level when cooling the camera below 0 °C can be seen. The noise level reaches its minimum at −30 °C. Further cooling of the camera increases the noise level, again.

3.7 Reference spectrometer

To investigate the absorption line shapes of interest with high resolution, the measured experimental spectra have to be divided by reference spectrum only showing the high-harmonic modulation. For this purpose reference spectra without the target gas have to be recorded. This extends the duration of the experiment by approximately a factor of two as for each experimental spectrum also a reference spectrum has to be recorded. This also makes the experiment more prone to fluctuations of the environmental conditions (temperature, humidity, laser power) which change the HHG spectrum on

almost all time scales, down to a single-shot level. To circumvent these problems, a Fourier approach has been developed [25] to filter out the spectrally broad modulation. This however can lead to artificial structures in the post-processed spectra.

As a new approach to get rid of the high-harmonic modulation, a reference spectrometer was designed for the new experimental setup. For this purpose, one of the gold mirrors of the split-mirror setup is replaced by a grating. For the zeroth order reflection, the grating acts like a plain mirror. This reflection order is therefore used to conduct the experiments. The first order reflection of the grating is coupled out into a reference spectrometer arm and is detected with an XUV camera identical to the one used in the high-resolution flat-field spectrometer. As the first order reflection does not interact with the target gas but is coupled out before, its spectrum is the desired reference spectrum.

4 Experiments

In this chapter the first experiments which were conducted with the setup described in chapter 3 are presented.

The NIR light pulses which are used to generate the high-harmonics spectra and perform the experiments are characterized using a d-scan [29], [30] setup.

First, the generated high-order harmonics spectra are depicted and discussed. Then some linear absorption spectra are shown with their typical absorption line shapes. Finally an NIR intensity scan is displayed wherein a clear change in the absorption line shape for different NIR intensities can be observed.

All of the spectra are recorded using the spectrometer introduced in chapter 3.6. To improve the signal-to-noise ratio and keep the recording times short, the hardware binning mode of the XUV camera is used. For this purpose the region where the harmonics hit the camera chip is selected and each column of pixels is vertically integrated.

4.1 Pulse characterization

The femtosecond NIR pulses from the laser system 3.1 are characterized using a dispersion-scan (d-scan) setup [29], [30]. The d-scan method is a simple and therefore also a very robust technique. The investigated pulses propagate through a pair of glass wedges and afterwards a nonlinear BBO crystal wherein a second-harmonic signal is generated. The second-harmonic spectra are recorded for different glass insertions. This delivers a two-dimensional trace from which the spectral phase and therefore also the pulse duration of the investigated pulses can be retrieved by an algorithm [29].

The d-scan characterization method provides information about the pulse shape, their duration and their spectral phase (see Figure 4.1).

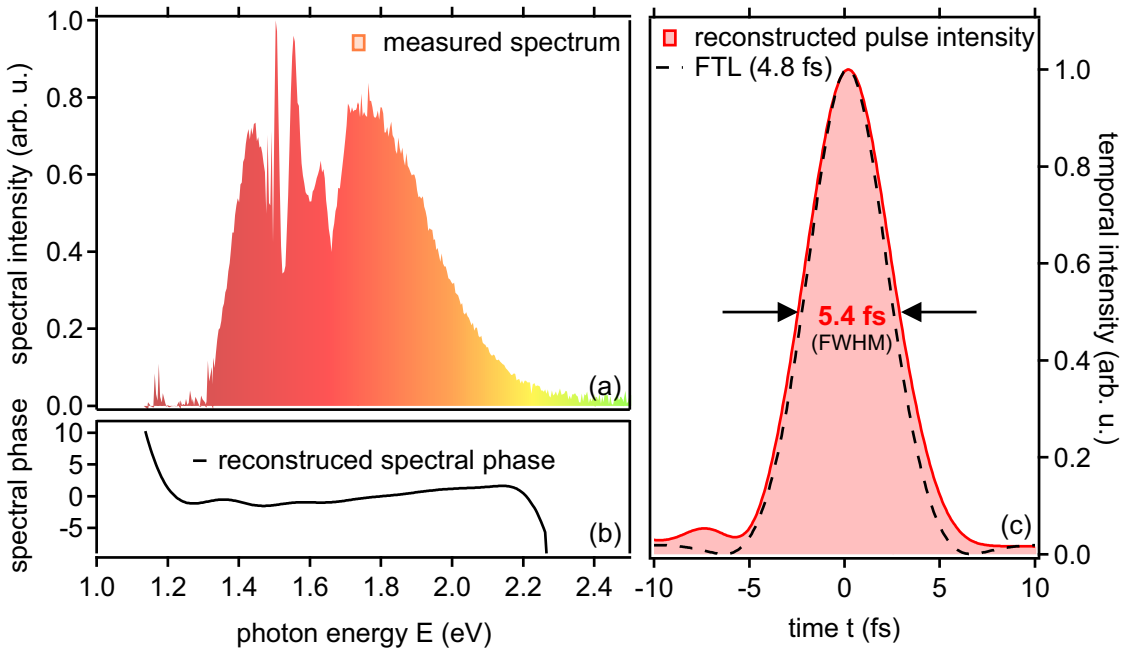

Figure 4.1: a: Measured spectrum of the NIR pulses. b: Their reconstructed spectral phase. c: Reconstructed pulse shape and duration as well as their Fourier-transformation limited (FTL) duration. This image is used with the kind permission of Alexander Blättermann.

4.2 High-harmonics spectra

For all of the proof of concept experiments presented in this chapter, XUV radiation produced by high-harmonic generation in Argon at a backing pressure of $\sim 75\,\mathrm{mbar}$ is used. As target Helium at a backing pressure of $\sim 60\,\mathrm{mbar}$ is used.

In Figure 4.2 the high-order harmonics spectra for two different openings of the motorized iris aperture (see chapter 3.3) are shown. They are denoted by the rotation stage positions of 75 and 83 where the former corresponds to an aperture opening of $\sim 8\,\mathrm{mm}$ and the latter is associated with an aperture opening of $\sim 5\,\mathrm{mm}$. A clear difference in the harmonics spectra can be seen. For the larger opening (see Figure 4.2 a)) a total of 8 harmonic orders can be seen. Four harmonic orders possess very similar intensities. These peaks nicely reveal the broad plateau region of equally intense harmonic orders (see also chapter 2.5). Higher harmonic orders with decreasing intensity appear as well. At an energy of $72.2\,\mathrm{eV}$ a sharp cutoff can be seen. At this energy the aluminum filter starts to absorb the XUV radiation. For the smaller aperture opening (see Figure 4.2b)) only 6 harmonic orders appear. The plateau region washes out and the overall intensity is reduced by about 30 %. At an energy of

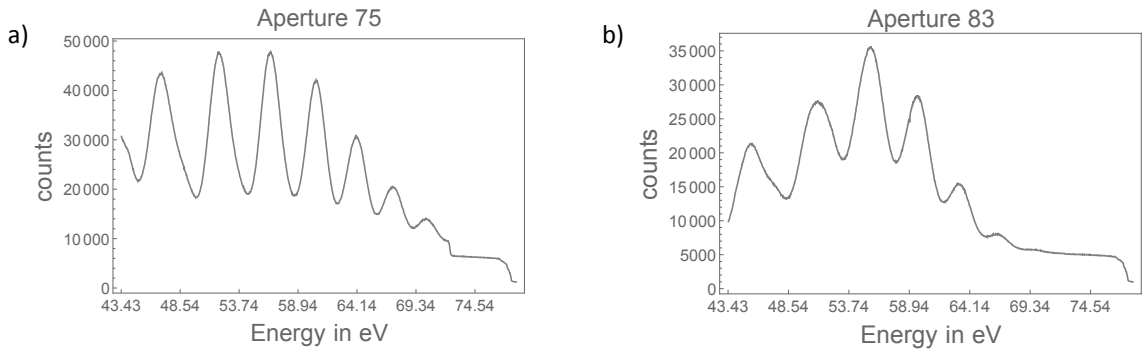

Figure 4.2: Two high-order harmonics spectra for different aperture openings of 75 (a) and 83 (b).

$\sim 70\,\text{eV}$ the XUV intensity drops to zero. In both spectra a background of ~ 6000 counts is clearly visible. This is due to incorrect alignment of the filter box (see Figure 3.11) and not optimal choice of the binning region, both of which increase the NIR background.

The fundamental differences in the high-order harmonics spectra reveal that a spatial chirp for the XUV radiation is apparent. Different photon energies appear across different positions of the XUV beam. One of the reasons could be deformations in the wavefront of the NIR driving field. This can lead to changing phase matching conditions across the generation spot.

4.3 Linear absorption spectra

Figure 4.3 shows a comparison of linear absorption spectra recorded in Helium using the high-harmonic radiation as described in chapter 4.2 (see Figure 4.2). The left column shows spectra recorded with an aperture position of 75, whereas the right column shows spectra recorded with an aperture position of 83. The topmost row shows the raw data which clearly resembles the high-harmonic spectra from Figure 4.2. The crucial differences are the absorption line shapes at an energy of $\sim 60.5\,\text{eV}$ and $\sim 64.2\,\text{eV}$ (the latter only visible for an aperture position of 83). The spectra are calibrated using the aluminum absorption edge at a photon energy of 72.2 eV [31] and the high-harmonic modulation which corresponds to twice the photon energy of the NIR pulses of $\sim 1.7\,\text{eV}$. The observed lines can be associated with the two lowest dipole-transition allowed doubly excited states of Helium at $60.1503(40)\,\text{eV}$ (2s2p) and $63.6575(30)\,\text{eV}$ ($\text{sp}_{2,3+}$) [32].

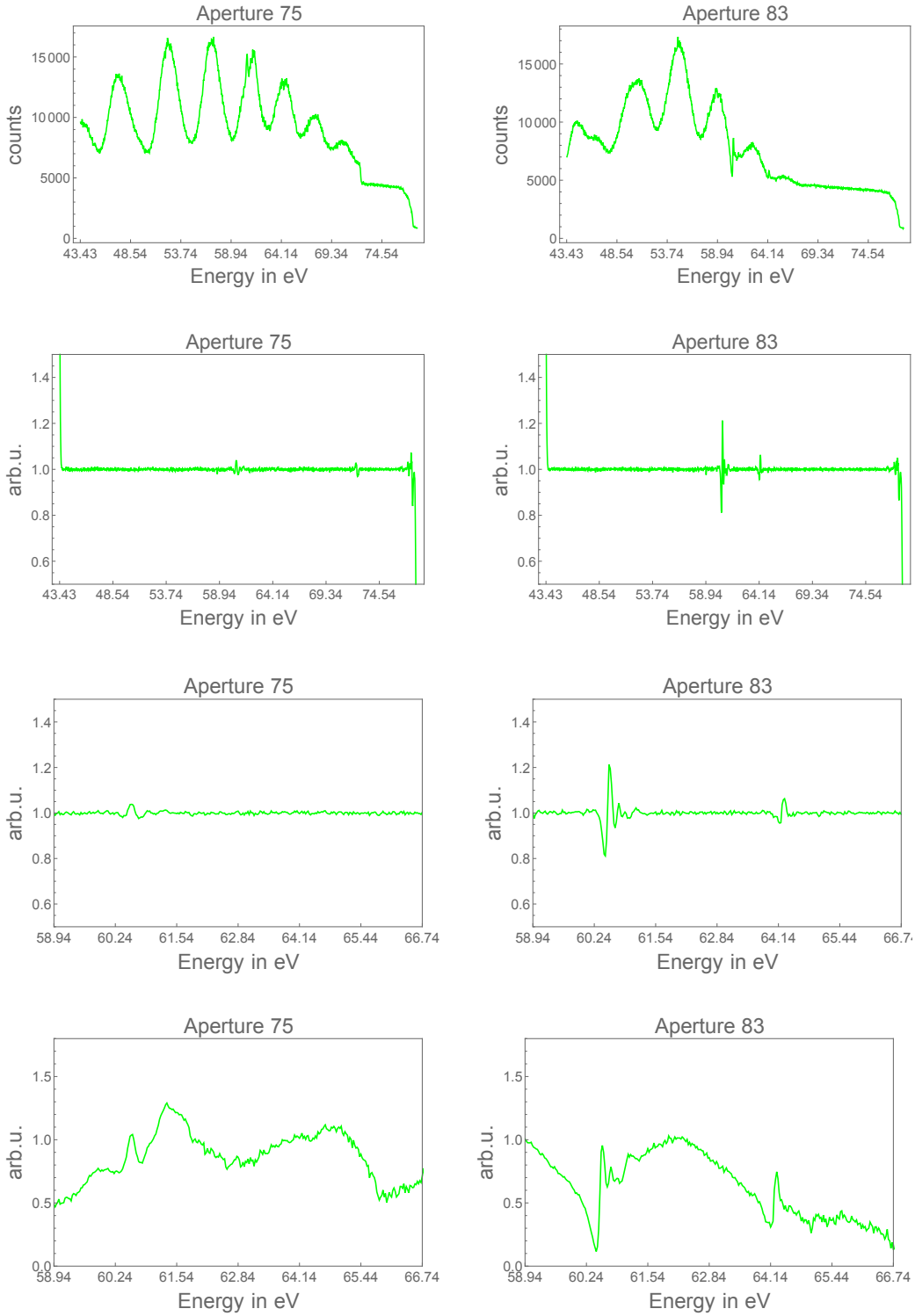

Figure 4.3: Shown are several transient absorption spectra of doubly-excited Helium for the two aperture positions of 75 and 83. First row: raw spectra. Second row: absorption spectra obtained after dividing the raw spectra by the Fourier-reconstructed reference spectrum. Third row: zoomed-in view of the second row. Fourth row: absorption spectra obtained for measured reference spectrum (note: harmonic modulation due to separate acquisition of absorption and reference spectrum). For details, see text.

The second row shows the spectra after applying a Fourier-filter to remove the high-harmonic modulation. The structures at the extreme edges of the spectra are artifacts due to this filtering. Furthermore the structure at the position of the Aluminum edge (72.2 eV) is an artifact due to the sharp cutoff. It vanishes for an aperture position of 83 since there is no XUV light at this chip position anymore (see Figure 4.2). The third row is a zoomed-in view of these spectra.

The fourth row shows the same spectra, however this time no Fourier-filter is used but they are corrected by dividing them by their reference spectra and subtracting the background (see chapter 3.7). It is important to note that strong fluctuations in the high-harmonic generation process give rise to unphysical modulations across these spectra. The additional reference spectrometer described in chapter 3.7 provides a good way to overcome this issue.

4.4 NIR intensity scan

Figure 4.4 shows an NIR intensity scan. The aperture position is varied from a position of 70 to a position of 83. This corresponds to aperture openings of 10 mm to 5 mm. Larger values hereby denote smaller aperture openings. A clear change in the absorption line shapes can be observed.

For large openings of the aperture the absorption lines nearly vanish (Figure 4.4, first row). This is a result of the strong-field ionization induced by the high-intensity NIR laser pulses. For smaller apertures an absorption line at an energy of ~ 60 eV appears (Figure 4.4, second row). Closing the aperture even further reveals three additional absorption lines above 64 eV. For the energetically lowest absorption line, a clear change in its shape can be observed. At larger aperture openings, corresponding to a higher NIR intensity, the line shape is symmetric. For smaller NIR intensities it changes into an asymmetric Fano line shape. This observation was analogously made in [17]. It nicely demonstrates the laser control of the dipole phase (see chapter 2.3 and Figure 2.3) as was shown by Ott et al. in [17]. This behaviour can also be observed for the absorption line shapes at higher photon energies.

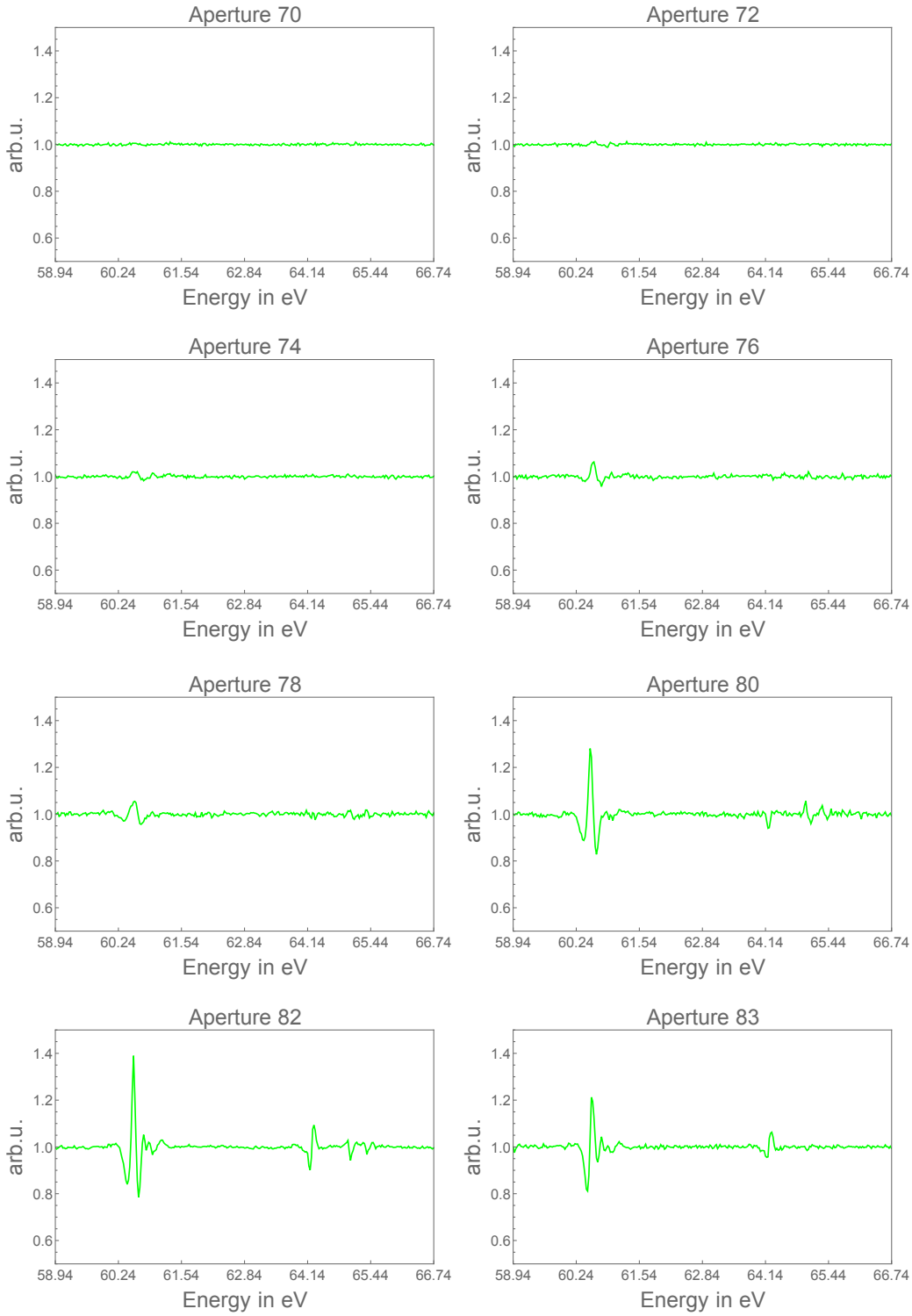

Figure 4.4: Transient absorption spectra of doubly-excited Helium. An NIR intensity scan was performed by varying the iris aperture openings. A clear change in the absorption line shape can be seen. For the highest NIR intensities, the absorption lines vanish due to strong-field ionization induced by the ultrashort, highly intense NIR pulses (first row). For lower NIR intensities the absorption lines have a symmetrical shape (rows 2 and 3). For the lowest NIR intensities the absorption lines reveal their natural asymmetric line shapes (row 4).

4.5 Initial alignment of the 4-quadrant split-mirror

The introduced 4-quadrant split mirror offers many degrees of freedom for the alignment procedure (see chapter 3.5). This is a big advantage, but at the same time demands a very precise alignment approach. It is crucial to find the spatial overlap between the single beams as well as the temporal overlap of the pulse trains.

As a first step to find the spatial overlap of the four beams a beam profiler was installed at the position of the experimental cell. All four beams are brought to overlap at this position using the tip/ tilt stages. The closed-loop stages allow to find this position again when operating with XUV radiation. Figure 4.5 shows the cross-shaped gaps between the individual 4 mirrors of the split mirror on the spectrometer camera (see chapter 3.6) when illuminated with XUV light. For this purpose the camera is moved to a position where the zeroth-order reflection of the grating can be recorded. The image also shows the contour of the motorized iris aperture. The mirror has to be aligned in a way that the iris cuts out the beam concentrically to the middle of the cross and the intensity is equally distributed over the four mirror segments. Figure 4.6 shows the corresponding high-order harmonic spectra. Naturally there are two rows of those spectra. One of the rows could be utilized in future experiments as a reference that does not pass through the experimental cell.

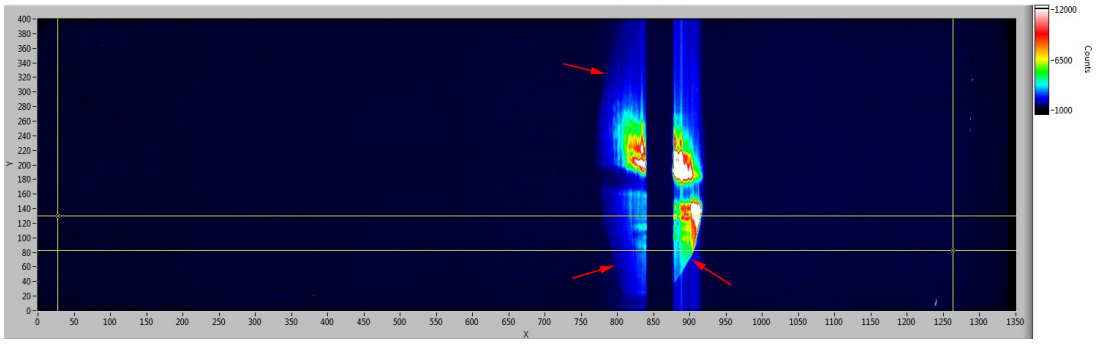

Figure 4.5: Cross-shaped shadow structure created by the gaps of the split mirror illuminated by XUV radiation. The image is recorded with the spectrometer camera using the zeroth-order reflection of the grating. The contour of the motorized iris aperture can also be seen in the image as marked by the arrows.

4.6 Finding temporal overlap and first time-delay scan

To find the temporal overlap of the NIR pulses, and therefore intrinsically also the temporal overlap of the XUV pulses, only two of the mirrors are used by simply

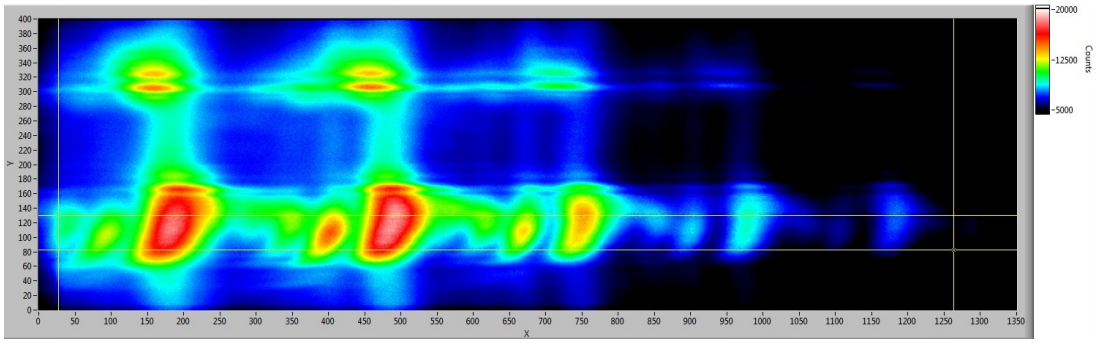

Figure 4.6: High-order harmonic spectrum of the beam in Figure 4.5.

elevating the entire mirror setup with the hexapod. This way, only the two lower mirrors are illuminated by the incident beam which this way is split into two identical beams. To optimize the spatial overlap, the zeroth order reflection of the XUV radiation is observed on the camera analogously to Figure 4.5. The experimental cell is moved perpendicular to the beam path. If one of the partial beams vanishes earlier than the other, the spatial overlap is not perfect. Using the tip/ tilt stages the spatial overlap can be optimized this way.

To find the temporal overlap of the lower two mirrors both of the delay stages are placed at their mid position of 125 µm. With this initial position, high-order harmonics are generated in Argon inside the experimental cell. Since high-order harmonic generation is a extremely nonlinear process, the intensity of these harmonics is strongly dependent on the temporal overlap of the generating NIR pulses. One mirror is fixed at its initial position of 125 µm. Scanning the other mirror leads to a large variation in the high-harmonic intensity. This way the temporal overlap of the two split beams is determined to a position of the scanned mirror of (125 ± 5) µm.

With the two beams in temporal and spatial overlap, a first time-delay scan is performed in steps of 5 µm corresponding to time steps of 8.6 fs (Figure 4.7). This rather coarse time-delay scan further indicates where a temporal overlap of the two beams exists [12].

Unfortunately, only small changes in the absorption lines can be observed at mirror positions close to the determined overlap at 125 µm compared to regions far away from the overlap (0 µm and 250 µm, see Figure 4.7). The changes can best be seen in the absorption lines at photon energies above 64 eV. Further investigations with a finer time-resolution have to be conducted at the overlap position in the future.

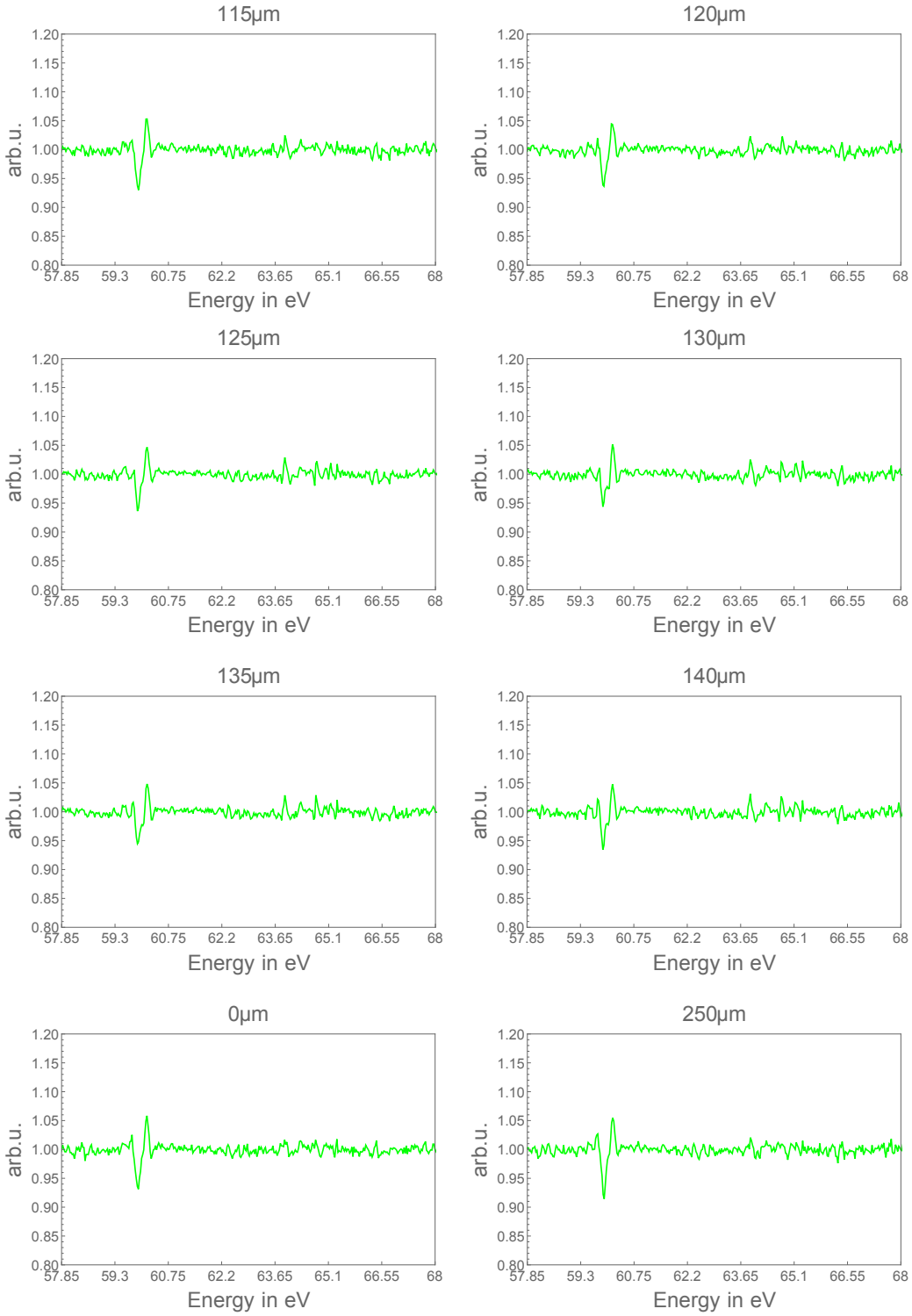

Figure 4.7: Time delay scan performed with two beams originating from the split-mirror setup. The step size of the delay stages of 5 µm translates into time steps of 8.6 fs. Only small changes in the absorption lines can be observed in the recorded spectra at overlap positions compared to mirror positions far away from temporal overlap.

5 Conclusion

The primary objective of this work was the design, construction and alignment of an experimental setup for multidimensional four-wave mixing spectroscopy in the extreme ultraviolet (XUV) and soft-X-ray spectral region. For this purpose a transient absorption spectroscopy setup was designed around a 4-quadrant split-mirror setup. This mirror allows to split an incident beam into four identical copies to perform four-wave mixing experiments.

The experimental setup is designed for the use at high-order harmonic sources as well as free-electron lasers (FEL). This allows to conduct a large number of different experiments. At high-order harmonic sources XUV-NIR spectroscopy experiments can be conducted. At FEL facilities it is also possible to perform XUV-XUV spectroscopy. With the designed experimental setup a further step to bring multidimensional four-wave mixing spectroscopy to the XUV spectral region was made. The high photon energies of XUV radiation of several tens of electron volts allow to investigate dynamical phenomena such as charge-migration dynamics or couplings between core-electron transitions in molecules.

As a proof of concept two experiments were conducted with the new experimental setup using a high harmonic source. For both experiments XUV radiation from HHG in Argon were used. These XUV pulses were then used to excite the doubly-excited states of Helium. For the first experiment the doubly-excited states were perturbed by an NIR pulse. The NIR intensity was varied to observe the well-known line shape changes from asymmetric Fano line shapes for the unperturbed case to symmetric Lorentzian line shapes for the strong-field perturbed case. In a second experiment two of the split mirrors were used to perform a time-delay scan in Helium and this way find the temporal overlap of the two generated pulsed beams.

Bibliography

[1] https://alumni.stanford.edu/get/page/magazine/article/?article_id=39117.

[2] Ahmed H. Zewail. Femtochemistry: Atomic-scale dynamics of the chemical bond. *J. Phys. Chem. A*, 104:5660–5694, May 2000.

[3] D. A. G. Deacon, L. R. Elias, J. M. Madey, G. J. Ramian, H. A. Schwettmann, and T. I. Smith. First operation of a free-electron laser. *Physical Review Letters*, 36(16), April 1977.

[4] B. D. Patterson and R. Abela. Novel opportunities for time-resolved absorption spectroscopy at the x-ray free electron laser. *Physical Chemistry Chemical Physics*, 12:5647–5652, May 2010.

[5] A. McPherson, G. Gibson, H. Jara, U. Johann, T. S. Luk, A. McIntyre, K.Boyer, and C. K. Rhodes. Studies of multiphoton production of vacuum-ultraviolet radiation in the rare gases. *J. Opt. Soc. Am B*, 4:595–601, April 1987.

[6] Anne L'Huillier, M. Ferry, L. A. Lompré, and G. Manfray. Multiple-harmonic generation in rare gases at high laser intensity. *Physical Review A*, 39(11), June 1989.

[7] Anne L'Huillier, Kenneth J. Schafer, and Kenneth C. Kulander. Theoretical aspects of intense field harmonic generation. *J. Phys. B: At. Mol. Opt. Phys.*, 24:3315–3341, 1991.

[8] Paul B. Corkum. Plasma perspective on strong-field multiphoton ionization. *Physical Review Letters*, 71(13), September 1993.

[9] G. Steinmeyer, D. H. Sutter, L. Gallmann, N. Matuschek, and U. Keller. Frontiers in ultrashort pulse generation: Pushing the limits in linear and nonlinear optics. *Science*, 286:1507–1512, November 1999.

[10] M. Hentschel, R. Kienberger, Ch. Spielmann, G.A. Reider, N. Milosevic, T. Brabec, P.Corkum, U. Heinzmann, M. Drescher, and F. Krausz. Attosecond metrology. *Nature*, 414:509–513, November 2001.

[11] M. Drescher, M. Hentschel, R. Kienberger, M. Uiberacker, V. Yakovlev, A. Scrinzi, Th. Westerwalbesloh, U. Kleineberg, U. Heinzmann, and F. Krausz. Time-resolved atomic inner-shell spectroscopy. *Nature*, 419:803–807, October 2002.

[12] Christian Ott, Andreas Kaldun, Luca Argenti, Philipp Raith, Kristina Meyer, Martin Laux, Yizhu Zhang, Alexander Blättermann, Steffen Hagstotz, Thomas Ding, Robert Heck, Javier Madroñero, Fernando Martín, and Thomas Pfeifer. Reconstruction and control of a time-dependent two-electron wave packet. *Nature*, 516:374–378, December 2014.

[13] Steven T. Cundiff and Shaul Mukamel. Optical multidimensional coherent spectroscopy. *Physics Today*, 66(7), July 2013.

[14] Igor V. Schweigert and Shaul Mukamel. Coherent ultrafast core-hole correlation spectroscopy: X-ray analogues of multidimensional nmr. *Physical Review Letters*, 99(163001), October 2007.

[15] Hans Beutler. Über absorptionsserien von argon, krypton und xenon zu termen zwischen den beiden ionisierungsgrenzen 2p 3/2 und 2p 1/2. *Zeitschrift für Physik*, 93:177–196, 1935.

[16] Ugo Fano. Effects of configuration interaction on intensities and phase shifts. *Physical Review*, 124(6), December 1962.

[17] Christian Ott, Andreas Kaldun, Philipp Raith, Kristina Meyer, Martin Laux, Jörg Evers, Christoph H. Keitel, Chris H. Greene, and Thomas Pfeifer. Lorentz meets fano in spectral line shapes: A universal phase and its laser control. *Science*, 340:716–720, May 2013.

[18] Alexander Blättermann, Christian Ott, Andreas Kaldun, Thomas Ding, and Thomas Pfeifer. Two-dimensional spectral interpretation of time-dependent absorption near laser-coupled resonances. *Journal of Physics B: Atomic, Molecular and Optical Physics*, 47, June 2014.

[19] P. Lambropoulos and P. Zoller. Autoionizing states in strong laser fields. *Physical Review A*, 24(1), July 1981.

[20] Nicolaas Bloembergen and Yuen-Ron Shen. Quantum-theoretical comparison of nonlinear susceptibilities in parametric media, lasers, and raman lasers. *Physical Review*, 133(1A), January 1964.

[21] Robert W. Boyd. *Nonlinear Optics*. Academic Press, 1. edition, 1992.

[22] Peter W. Milonni and Joseph H. Eberly. *Lasers*. John Wiley & Son's, Inc., New York, 1. edition, 1988.

[23] Leonid V. Keldysh. Ionization in the field of a strong electromagnetic wave. *Soviet Physics JETP*, 20(5), May 1965.

[24] Christian Ott. *Attosecond multidimensional interferometry of single and two correlated electrons in atoms*. PhD thesis, Ruperto-Carola-University of Heidelberg, July 2012.

[25] Andreas Kaldun, Christian Ott, Alexander Blättermann, Martin Laux, Kristina Meyer, Thomas Ding, Andreas Fischer, and Thomas Pfeifer. Extracting phase and amplitude modifications of laser-coupled fano resonances. *Physical Review Letters*, 112(103001), March 2014.

[26] Bahaa E. A. Saleh and Malvin Carl Teich. *Fundamentals of Photonics*. Wiley, 2 edition, 2007.

[27] http://newport.com/.

[28] Veit Stooß. Time-resolved strong field effects in helium observed with transient absorption spectroscopy. Master's thesis, Ruperto-Carola-University of Heidelberg, 2015.

[29] Miguel Miranda, Thomas Fordell, Cord Arnold, Anne L'Huillier, and Helder Crespo. Simultaneous compression and characterization of ultrashort laser pulses using chirped mirrors and glass wedges. *Optics Express*, 20(1):688–697, January 2012.

[30] Miguel Miranda, Cord L. Arnold, Thomas Fordell, Francisco Silva, Benjamín Alonso, Rosa Weigand, Anne L'Huillier, and Helder Crespo. Characterization of broadband few-cycle laser pulses with the d-scan technique. *Optics Express*, 20(17):18732–18743, August 2012.

[31] http://henke.lbl.gov/optical_constants/filter2.html.

[32] K. Schulz, G. Kaindl, M.Domke, J.D. Bozek, P.A. Heimann, A.S. Schlachter, and J.M. Rost. Observation of new rydberg series and resonances in doubly excited helium at ultrahigh resolution. *Physical Review Letters*, 77(15):3086–3089, October 1996.